Title

Activating magnetite ores for aqueous ironmaking at high current densities

Journal

Energy & Environmental Science

ISSN

1754-5692

Authors

Shekhar, Raj

Cecil, James A

Goldman, Andrew C

et al.

Publication Date

2026

DOI

10.1039/d6ee01056c

Activating magnetite ores for aqueous ironmaking at high current densities

Raj Shekhar,[1,2] James A. Cecil,[1,2] Andrew C. Goldman,[1,2] Evandi Rahman,[1,2] Louka J. Moutarlier,[1,2] Faiqa Khaliq,[1] Audrey Davenport,[1] Shannon W. Boettcher,[3] Paul A. Kempler[1,2*]

[1]Department of Chemistry and Biochemistry, University of Oregon, Eugene, OR, USA
[2]The Oregon Center for Electrochemistry, University of Oregon, Eugene, OR, USA
[3]Department of Chemical & Biomolecular Engineering and Department of Chemistry, University of California, Berkeley, CA, USA

*Correspondence: pkempler@uoregon.edu

Abstract:

Low-temperature electrochemical cells reducing iron oxides to metal in alkaline electrolytes can support fully electrified steelmaking processes. Previous studies on these cells have primarily focused on high-surface-area hematite, Fe_2O_3, reactants whereas attempts to reduce suspensions of magnetite, Fe_3O_4—one of the two feedstocks for existing ironmaking reactors—have generally been limited to low rates of reaction (<30 mA cm^{-2}). Here, we control the crystalline domain size of Fe_2O_3 and Fe_3O_4 particles in 10 M NaOH electrolytes to study how the nanoscale morphology of oxides controls the rate of electrochemical ironmaking. Rotating-ring disk electrode measurements of Fe^{2+}, *in-situ* Raman spectroscopy of the electrode surface, and *ex–situ* electron microscopy were consistent with a hypothesized passivation process at Fe_3O_4 surfaces that may prevent the continuous formation of soluble intermediates. Sufficiently small (<100 nm diameter) oxide particles yielded Fe partial current densities > 160 mA cm^{-2}, a fivefold increase relative to previously reported rates for Fe_3O_4 suspensions and comparable to active Fe_2O_3. Electron microscopy revealed that electrodeposited films were composed of micron-scale crystalline Fe domains with a porous film of Fe_3O_4 nanoparticles and supports a model where Fe is grown primarily from soluble Fe^{2+} intermediates. Based on these insights, inactive blast-furnace-grade iron-oxides were transformed into high surface area nanoparticles (1.6 to 229.2 $m^2\ g^{-1}$) via reprecipitation, leading to a ninefold enhancement in faradaic efficiency and an Fe partial current density of 120 mA cm^{-2}. When integrated with chlor-iron cells producing reagents for reprecipitation, this approach could lead to a cost-competitive process for electrochemical ironmaking from industrially relevant feedstocks.

Keywords: magnetite, hematite, iron metal, TEM, nanoparticles

Introduction:

Metallic iron (Fe) is a vital commodity for steel production and a critical component of proposed approaches to long-duration energy storage.[1–6] Most Fe produced today is reduced in blast furnaces at >1400 °C with carbon monoxide (CO) serving as the chemical reductant, ultimately producing 7% of global carbon emissions.[7,8] Processed iron oxide ores from a wide variety of sources serve as precursors in the blast furnace but hematite (α-Fe_2O_3) and/or magnetite (Fe_3O_4) are most typical and a representative expression for reduction is:[9,10]

$$Fe_xO_y + yCO \rightarrow xFe + yCO_2 \qquad (\mathbf{1})$$

In a blast furnace, molten Fe is the product and gangue impurities (Si, Ca, Mg, etc…) can be removed as a physically separated slag. The direct-reduced iron, DRI, process occurs at lower temperatures, may in principle operate with hydrogen or ammonia serving as reducing agents, and maintains both iron reactants and products in the solid state.[11–13] When Fe is produced as a solid product, the purity requirements and phase of the iron oxide reactants are more stringent.[14] A feed containing α-Fe_2O_3 ore is most often used for the DRI process; dense Fe_3O_4 ores exhibit slower reduction kinetics due to constraints on the diffusion of gas reactants.[15]

Ironmaking can be directly electrified through the use of electrochemical cells. If these reduction processes are powered by zero-carbon electricity sources they could help eliminate carbon emissions associated with steelmaking. Iron can be grown from low-temperature, acidic electrolytes after dissolution from iron ores or produced as a solid or liquid product from molten salts.[16–19] An alternate approach involves the use of concentrated alkaline electrolytes which facilitate the direct reduction of solid iron oxides to iron metal at moderate temperatures < 120 °C.[20–22] The direct reduction pathway supports conversion at high rates (hundreds of mA cm^{-2}) in the

absence of forced convection and does not require operation at high temperatures, both of which could support lower costs for cell construction. When isolated by a selective membrane, the reduction of iron oxides in alkaline electrolytes also leads to the coproduction of hydroxide as a co-product (equations 2–3).[23] However, the solid-to-solid conversions means that the phase and purity of the reactant iron oxide has a substantial impact on the reaction kinetics and product purity, with powdered α-Fe_2O_3 affording the most rapid and selective reduction to Fe:[24]

$$2\ Fe_2O_3 + 3\ H_2O + 6\ e^- \rightarrow 4\ Fe + 6\ OH^- \quad (\mathbf{2})$$

Fe_3O_4 reactants have consistently yielded lower rates and selectivity for Fe metal formation[22,25]:

$$Fe_3O_4 + 4\ H_2O + 8\ e^- \rightarrow 3\ Fe + 8\ OH^-(aq) \quad (\mathbf{3})$$

Nevertheless, Fe_3O_4 comprises nearly one quarter of the world's iron ores,[26] and can be more easily freed from gangue impurities through magnetic separation. Understanding and resolving the differences in reactivity for these two oxides would expand the scope of one of the most-promising electrified reactions for ironmaking.

The mechanism of iron oxide reduction has been discussed either as a solid-state reaction, or a dissolution-redeposition pathway.[20,27,28] Recent rotating ring-disk electrode (RRDE) and correlated microscopy results suggest that morphology influences the dominant pathway for α-Fe_2O_3 reduction in aqueous medium.[29] Porous α-Fe_2O_3 particles produce a greater fraction of soluble ferrous intermediates than dense α-Fe_2O_3, and these intermediates prove to support facile Fe growth.[24]

Previous studies have reported the presence of magnetite in partially reduced hematite films, suggesting that it may act as a reaction intermediate in concentrated alkaline electrolytes.[30] Magnetite is also observed during the solid-state reduction of hematite under hydrogen gas[31] and

ex-situ Mossbauer was used to show the presence of magnetite in the electrochemically reduced pellet of α-Fe_2O_3.[20] However, Fe_3O_4 can also be formed during the spontaneous oxidation of Fe metal and the cubic structure of iron oxide layers observed in XRD and TEM analysis could also be attributed to a γ-Fe_2O_3 phase, leaving the identity and role of oxides observed only *ex-situ* in question.[32,33] We hypothesized that the observed difference in the kinetics between α-Fe_2O_3 and Fe_3O_4 is primarily due to the transport environment at the metal/metal oxide interface, and that this fact has been overlooked due to the wide range of particle sizes and/or poorly defined interfaces used in most studies on direct alkaline reduction of iron oxides.

In this study, we address these experimental gaps by preparing a set of high-purity and morphologically similar *α*-Fe_2O_3 and Fe_3O_4 samples to investigate how morphology affects the kinetics of iron oxide reduction. We first synthesized Fe_3O_4 nanoparticles and used these as a feedstock for homologous α-Fe_2O_3 via thermal oxidation. The mechanism during conversion of both *α*-Fe_2O_3 and Fe_3O_4 was probed with thin-film cyclic voltammetry (CV) and RRDE where the dissolution products from the disk could be measured directly on a ring electrode. Scan-rate-dependent voltammetry was used to study the kinetics of the oxide reduction process. The results were translated to a model electrowinning environment using batch-cell electrolysis which identified active phases for Fe production at high rates. Based on these findings, we designed a new reprecipitation method to convert blast furnace powders (BET surface area = 3.5 $m^2\ g^{-1}$) to high-surface-area Fe_3O_4 particles of gravimetric surface area of 229.2 $m^2\ g^{-1}$, which yielded $|j_{Fe}|$ of 119 mA cm^{-2}, among the highest reported rates of Fe production from an iron ore. A technoeconomic analysis based on this process was conducted to identify geographic regions where reprecipitation and electrowinning can be used to produce cost-competitive iron metal for steelmaking.

Results:

Role of soluble Fe^{2+} on the reduction kinetics

High purity α-Fe_2O_3 particles (*pc*-Fe_2O_3, **Fig. S1-S2**) were synthesized using a previously reported sol-gel method (**Supporting Information**)[34] with a subset of particles annealed at 1000 °C under N_2 atmosphere to obtain a dense α-Fe_2O_3 phase (*an*-Fe_2O_3, **Fig. S1, S3**). The annealing process preserved the nominal particle size (0.8–1.3 μm) but reduced the surface area measured by gas sorption from 29.4 m^2 g^{-1} as prepared to 1.3 m^2 g^{-1} after annealing, which is comparable to typical iron ores (**Table S1)**. These particles were compared to a blast-furnace-grade iron oxide powder (*bf*-Fe_3O_4) which consisted of polydisperse particles ranging from 200 nm to 50 μm and which yielded a BET surface area of 1.6 m^2 g^{-1} (**Fig. S4**). XRD measurements showed that these particles were predominately Fe_3O_4 (**Fig. S5**) and energy-dispersive X-ray (EDX) analysis indicated the presence Ca, Al, Mg, and Si impurities in >12% of the total Fe content (**Table S2**).

Figure 1 compares the electrochemical response of thin films of iron oxide with different phases and morphologies compared against the faradaic efficiency towards Fe metal (η_{Fe}) during a controlled current electrolysis at –200 mA cm^{-2}. Thin films of *pc*-Fe_2O_3 at a glassy-carbon disk yielded cathodic currents > 2 A g^{-1} at E = –1.0 V (**Fig. 1a**), with currents of –10 A g^{-1} at E = –1.15 V. This was accompanied by a gradual onset of the ring current corresponding to one-electron Fe^{2+} oxidation (**Fig. 1b**). In contrast, *an*-Fe_2O_3 and *bf*-Fe_3O_4 films were unreactive at E > –1.1 V, and only *an*-Fe_2O_3 yielded a sharp ring-current peak, which was previously correlated with the particle fracture under the compressive stress during metal formation.[29] The faradaic efficiency towards

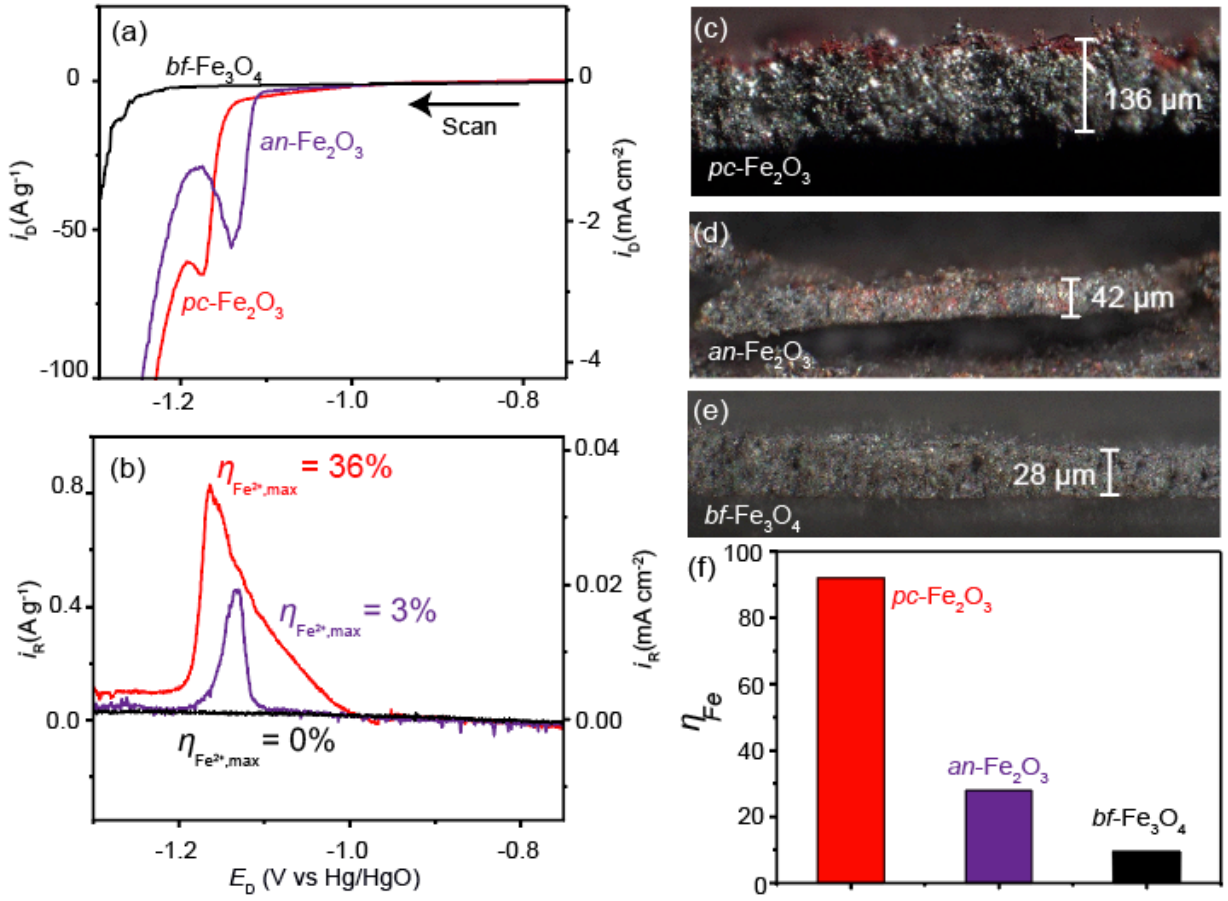

Figure 1: Electrochemical comparison of different phases and morphology of iron-oxide. Thin-film RRDE of α-Fe_2O_3 and *bf*-Fe_3O_4. (a) LSV at the disk at 5 mV/s. (b) Ring current (-0.3 V vs Hg/HgO) Cross-sectional optical images of Fe film produced from (c) *pc*-Fe_2O_3, (d) *an*-Fe_2O_3 and (e) *bf*-Fe_3O_4. (f) Faradaic efficiency for Fe metal during iron-oxide electrolysis at –200 mA cm^{-2} for 20 min at 82 °C in 30% w/w NaOH. Porous iron-oxide particles show higher $\eta_{Fe^{2+}}$ and η_{Fe}.

soluble Fe^{2+} ($\eta_{Fe^{2+}}$) detected at the ring was calculated as $\eta_{Fe^{2+}} = \frac{i_D}{i_R N_C}$, where N_c is the collection efficiency ($36 \pm 4\%$), estimated using a $Ru^{2+/3+}$ couple (as $RuCl_3$) in 30% w/w NaOH (**Fig. S6**). The maximum $\eta_{Fe^{2+}}$ for *pc*-Fe_2O_3 was 36%, compared to 3% and 0% for *an*-Fe_2O_3 and *bf*-Fe_3O_4 respectively (**Fig. 1b**).

Bulk reduction of suspended iron oxide powders at –200 mA cm^{-2} in 30% w/w NaOH at 82 °C enabled comparisons of the reactivity of iron oxide phases at an active metal surface relevant to iron electrowinning. Optical images of as-grown Fe films were used to compare the thickness of films after equivalent amounts of charge had been passed (**Fig. 1c-e**), and the gravimetric faradaic efficiency was calculated assuming a 3 e^- reduction for Fe_2O_3 and a 2.67 e^- reduction for Fe_3O_4. Electrolysis of *pc*-Fe_2O_3 yielded a greater η_{Fe} (92%) and thickness (136 μm) compared to *an*-Fe_2O_3 (η_{Fe} = 28%, 42 μm) and *bf*-Fe_3O_4 (η_{Fe} = 7.5%, 28 μm) (**Fig. 1g**), and both of these figures of merit were positively correlated with $\eta_{Fe^{2+}}$ measured in rotating-ring-disk experiments.

Comparisons of homologous Fe_2O_3 and Fe_3O_4 particles

The set of morphologically well-defined nanoparticles of Fe_3O_4 (*np*-Fe_3O_4) and Fe_2O_3 (*np*-Fe_2O_3) synthesized here allowed for a direct investigation of how the crystalline phase of dense oxide particles influences the conversion behavior in alkaline electrolytes. The *np*-Fe_3O_4 particles were precipitated from $Fe(NO_3)_2$ solutions to yield high-purity nanoparticles of Fe_3O_4, less than 200 nm in diameter (**Supporting Information**).[35] A subset of these particles were annealed at 650 °C for 10 h under air to obtain a homologous set of α-Fe_2O_3 particles (*np*-Fe_2O_3, **insets of Fig. 2c,d**). These particles were characterized by XRD and Raman spectroscopy, which indicated that the particles could be described as phase-pure α-Fe_2O_3 particles which maintained the original shape and size of the precipitated Fe_3O_4 (**Fig. 2a,b**). TEM and HRTEM images of both *np*-Fe_3O_4

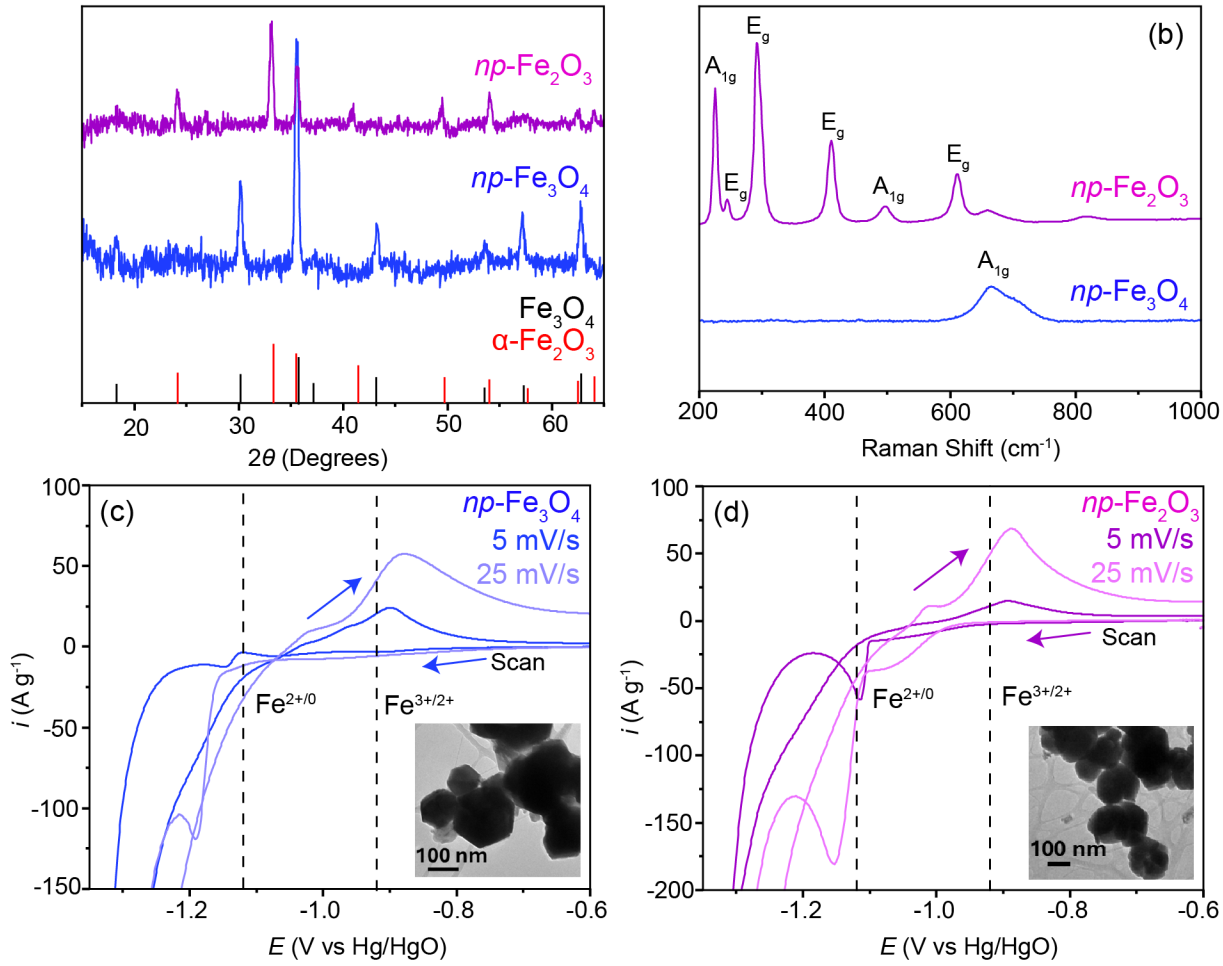

Figure 2: Material and electrochemical characterization of iron-oxide nanoparticles. (a) XRD of *np*-Fe_3O_4 and *np*-Fe_2O_3. (b) Raman spectra of *np*-Fe_3O_4 and *np*-Fe_2O_3. (c,d) Scan-rate dependent CVs of (c) *np*-Fe_3O_4 and (d) *np*-Fe_2O_3. A constant mass loading of 43 µg cm^{-2} was drop-cast on the GC electrode, which served as the working electrode in 30% w/w NaOH at 90 °C. Inset images in (c,d) represent the bright field TEM images of *np*-Fe_3O_4 and *np*-Fe_2O_3. Scan-rate normalized peak current density at 25 mV/s and 5 mV/s for *np*-Fe_3O_4 and *np*-Fe_2O_3. Dashed lines represent the formal potential of $Fe^{3+/2+}$ and $Fe^{2+/0}$ couple. Morphologically similar Fe_3O_4 and Fe_2O_3 yield different scan-rate dependent current responses.

and *np*-Fe_2O_3 showed that the particles were crystalline and lacked amorphous regions (**Fig S7-S8**). The surface of *np*-Fe_3O_4 showed atomic fringes along the <311> zone axis, while the bulk showed a single-crystalline diffraction pattern (**Fig. S7c,d**). Similarly, the surface of *np*-Fe_2O_3 exhibited well-defined atomic fringes (assigned to the <012> direction) and the diffraction pattern

collected at the center of the particle showed that individual particles were highly crystalline (**Fig. S8b,c**).

Scan-rate-dependent thin-film voltammetry was used to examine the multi-electron reduction process of different phases of iron oxides, with all data collected on the first scan of a freshly drop cast iron oxide film. This ensured that the reactant oxide morphology was well defined during measurements of the irreversible conversion to Fe metal. **Figure 2** shows the scan-rate-dependent voltammetry of *np*-Fe_3O_4 and *np*-Fe_2O_3 under equivalent reduction conditions. At slow scan rates, 5 mV s^{-1}, *np*-Fe_3O_4 films yielded three reduction waves at –0.92 V, –1.1 V and –1.15 V (**Fig. S9**), which indicate separate surface transformations, whereas only two reduction waves were observed at 25 mV s^{-1}, –1.0 V and –1.19 V. The cathodic peak at potentials where Fe^0 formation can occur increased nearly ten-fold from –13 A g^{-1} to –120 A g^{-1} (**Fig. 2c**). Further increases to the scan rate caused the peak current to increase from 550 A g^{-1} at –1.3 V to 3,500 A g^{-1} at –1.28 V and the total charge passed to increase from 0.68 mC at 5 mV s^{-1} to 2.0 mC at 500 mV s^{-1} (**Fig. S10a, Fig. S11a**). Assuming the integrated charge at 0.8 V> E > –1.23 V could be assigned to the overall Fe_3O_4 to Fe reaction (**Eq. 3**), these charges were equivalent to a 6.3% and 19% reduction of the Fe atoms within the film, at 5 and 500 mV s^{-1}, respectively. Clearly, the electrochemical reduction of Fe_3O_4 particles was inhibited during slow conversion to Fe and accelerated during fast potential sweeps.

In contrast to *np*-Fe_3O_4, *np*-Fe_2O_3 films yielded two reduction waves at 5 mV s^{-1}. (**Fig. 2d**) The onset of the first wave occurred at –0.85 V, and a second reduction wave yielded a peak at –1.1 V with a gravimetric current density of 60 A g^{-1}. Both waves were clearly resolved at 25 mV s^{-1}, with a peak current density of –181 A g^{-1} occurring at –1.15 V (**Fig. 2d)**. At faster scan rates (100 and 500 mV s^{-1}), peaks were no longer resolved but the current onset remained consistent (

Fig. S10b). In contrast to *np*-Fe_3O_4, which exhibited an increased extent of reduction with increasing scan rate, *np*-Fe_2O_3 showed more typical signs of a kinetically limited reduction process where the total charge passed was inversely proportional to the scan rate (**Fig. S11b**). For *np*-Fe_2O_3, 2.65 mC of charge was passed at 5 mV s^{-1}, enough to reduce ~25% of the film, whereas 1.29 mC cathodic charge was passed at 500 mV s^{-1}. This highlighted the unique behavior of Fe_3O_4 particles during conversion in alkaline electrolytes, as compared to other metal oxide particles of similar diameter and surface area.

Thin-film RRDE of homologous iron-oxides

A glassy-carbon ring electrode was selective for Fe^{2+} oxidation at –0.3 V vs Hg/HgO and facilitated direct measurements of soluble Fe^{2+} which are involved in the conversion mechanisms. **Figure 3a,d** show the thin-film voltammetry response of *np*-Fe_3O_4 and *np*-Fe_2O_3 at 1000 rpm, in 30% w/w NaOH at 90 °C, at various scan rates. Cathodic current at the disk at E_D > -1.3 V was attributed to formation of Fe^{2+} in the solid or aqueous phase whereas anodic currents were assigned to oxidation of aqueous Fe^{2+}. The peak currents from *np*-Fe_2O_3 towards $Fe^{3+/2+}$ and $Fe^{2+/0}$ increased with increasing scan rate and was three times that observed for *np*-Fe_3O_4 (**Fig. 3a, d**). **Figure 3b,e** show the ring current behavior during iron-oxide reduction. Both the onset of cathodic current and the onset of Fe^{2+} production from *np*-Fe_3O_4 films shifted towards negative *E* with increasing scan rates, which was not observed for *np*-Fe_2O_3 films, consistent with slower reduction kinetics for *np*-Fe_3O_4 (**Fig. 3a-b, d-e**). Interestingly, both *np*-Fe_3O_4 and *np*-Fe_2O_3 films yielded only a single reduction wave with no resolved peak at 100 mV s^{-1} (**Fig. S12**). Consistent with the thin-film response of *np*-Fe_3O_4 and *np*-Fe_2O_3, the cathodic charge passed during *np*-Fe_3O_4 reduction increased with increasing scan rates, while cathodic charge for *np*-Fe_2O_3 decreased with increasing scan rate (**Fig. S12**). The maximum value $\eta_{Fe^{2+}}$ obtained from *np*-Fe_3O_4 films increased from 40% to 80%

when the scan rate was increased from 5 mV/s to 10 mV/s. In contrast, the ring current from *np*-Fe_2O_3 films was independent of scan rate for 5 to 25 mV/s, with a similar onset to the disk current

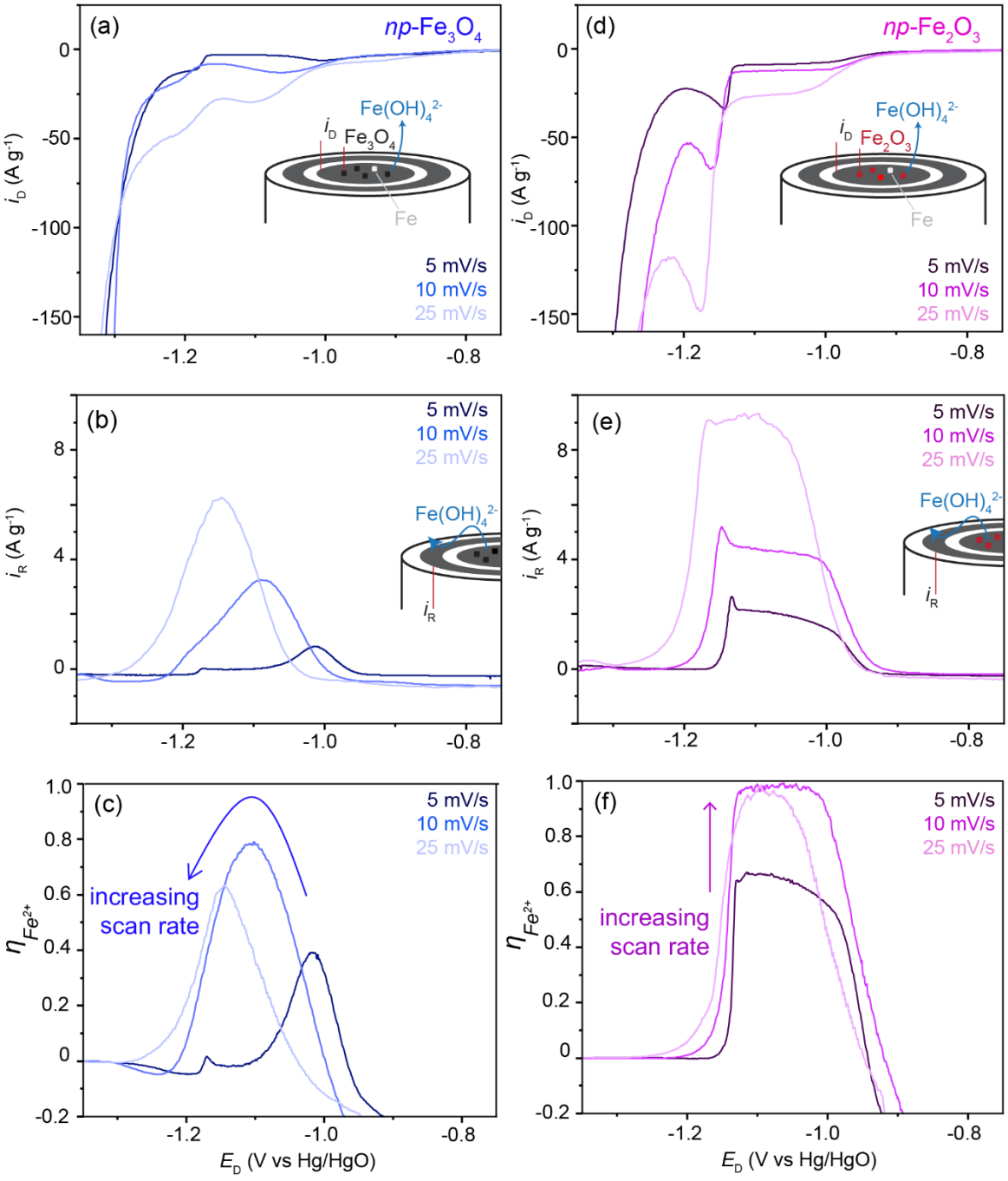

Figure 3: Thin-film rotating-ring-disk of iron-oxide nanoparticles. RRDE of thin film (**a,b,c**) *np*-Fe_3O_4 and (**d,e,f**) *np*-Fe_2O_3 (mass loading: 43 µg cm^{-2}) in 30% w/w NaOH at 90 °C. (a,d) Disk current and (b,e) ring current (E = –0.3 V) during negative potential sweep. (c,f) The fraction of soluble Fe^{2+} ($\eta_{Fe^{2+}}$) formation. The rotation rate was 1000 rpm. The reductive dissolution behavior is different for Fe_2O_3 and Fe_3O_4.

followed by a plateau and then decline to zero current at potentials sufficiently negative to form Fe metal. Moreover, the maximum value of $\eta_{Fe^{2+}}$ for *np*-Fe_2O_3 increases from 62% at 5 mV/s to almost 100% at 10 and 25 mV/s. At a scan rate of 100 mV/s, the ring current peak was diminished, qualitatively consistent with the behavior of *np*-Fe_3O_4 (**Fig. S12**).

The phase of the reactant iron oxide had a significant impact on the potential-dependence of soluble Fe^{2+} collection. The onset of Fe^{2+} collection at the ring shifted to more negative *E* with increasing scan rates for *np*-Fe_3O_4, but this onset was independent of the scan-rate for *np*-Fe_2O_3 (**Fig. 3b, e**). For both oxides, Fe^{2+} was no longer detected at values of *E* where Fe metal formation is expected to occur at the disk. The ring-current response of *np*-Fe_3O_4 was also sensitive to the cell temperature and NaOH concentration (**Fig. S13**). The ring-current onset shifted towards positive *E* with increasing temperature, shifting from $E = -0.98$ V at 80 °C to $E = -0.94$ V at 110 °C, and this was accompanied by an increase in the current plateau at $E > -1.2$ V to ~0.5 A g^{-1}, compared to ~0 at 80 °C (**Fig. S13b**). Fe_3O_4 films reduced in 50% w/w NaOH yielded a greater quantity of aq. Fe^{2+} and a decrease in the Fe^{2+} collection current prior to the formation of Fe metal was no longer observed (**Fig. S14**). Increasing both the temperature to 110 °C and [NaOH] to 50% w/w led to a threefold increase in the amount of total aq. Fe^{2+} collected from Fe_3O_4 films (**Fig. S15**).

Measurement of soluble Fe^{2+} generated during the oxidation of Fe revealed differences in the morphology of Fe metal formed from Fe_3O_4 and Fe_2O_3. Linear sweep voltammogram (LSV) of both *np*-Fe_3O_4 and *np*-Fe_2O_3 yielded an anodic peak at –0.9 V, with three times as much charge passed during oxidation in case of *np*-Fe_3O_4, compared to *np*-Fe_2O_3 (**Fig. S16**). The current at the ring, which was again biased at –0.3 V, showed a positive current, indicating that aq. Fe^{2+} was formed at $E < -0.8$ V, and the absence of current for $E > -0.8$ V, was more consistent with the formation of insoluble $Fe^{2+/3+}$ compounds fully oxidized aq. Fe^{3+}. During the anodic sweep of *np*-

Fe_3O_4, 237 μC of charge was passed at the disk, while the ring only accounted for 10.4 μC, which signifies an $\eta_{Fe^{2+}}$ of merely 12% (considering 36% collection efficiency). On the other hand, 73 μC and 6.6 μC charges were passed on the disk and ring, respectively, for *np*-Fe_2O_3 resulting in an $\eta_{Fe^{2+}}$ of 25%.

In-situ Raman spectroscopy of iron oxides

Figure 4 shows in-situ Raman spectra collected on *np*-Fe_3O_4 and *np*-Fe_2O_3 during conversion in 30% w/w NaOH at 60 °C under controlled potentials performed to identify insoluble intermediate oxides. In-situ Raman experiments were collected in immersion mode with an objective protected by a 13 μm thin PTFE film (**Fig. 4a and Fig. S17**) adjacent to iron oxide nanoparticles deposited on an Au working electrode. Prior to electrochemical reduction, *np*-Fe_3O_4 films biased at –0.8 V produced a prominent peak at 671 cm^{-1} that was be assigned to Fe_3O_4. The spectra were essentially unchanged at increasingly negative potentials, up to –1.1 V, aside from a slight decrease in intensity. At –1.15 V, the peak at 671 cm^{-1} was replaced by two new peaks at 538 cm^{-1} and 815 cm^{-1} (**Fig. 4b, Fig. S18**). When the bias was reversed, from –1.2 V to –0.3 V, these new peaks were diminished and the peak at 670 cm^{-1}, corresponding to Fe_3O_4, returned as the most prominent Raman peak (**Fig. S19**).

Films of *np*-Fe_2O_3 in 60 °C and 30% w/w NaOH and biased at E = –0.8 V yielded a trio of Raman peaks from 200 to 450 cm^{-1} which were consistent with phase-pure α-Fe_2O_3 (**Fig. 4c**). During a controlled set of potential steps to –1.3 V the peaks gradually disappeared, and no new phases were detectable in the Raman spectra, in contrast to the behavior observed for *np*-Fe_3O_4 films. During electrochemical reduction, a grayish precipitate formed on the Au surface, and this was accompanied by the production of gas bubbles assumed to be H_2. Following the production

of Fe metal, the working electrode was returned to a more oxidizing potential (–0.8 V) and a peak at 670 cm^{-1} was observed which was assigned to Fe_3O_4 (**Fig. S20**).

Next, ex-situ TEM characterization was performed on *np*-Fe_3O_4, drop cast on a Au TEM grid and reduced at –1.1 V at 90 °C and 30% w/w NaOH. An amorphous layer of ~3–4 nm was observed around the partially reduced particle. The bulk of the particle appeared to be crystalline and had a d-spacing of 2.93 Å, which is consistent with the (220) facet of Fe_3O_4 (**Fig. S21**).

Ex-situ SEM and TEM analysis of Fe films prepared from different iron oxides

Figure 5a-d show scanning electron microscopy (SEM) images of iron metal films produced from iron oxide nanoparticles in 30% w/w NaOH at 82 °C at a constant current density of −200 mA cm^{-2} for 1 h. A porous layer of nanoscale iron oxide particles formed on the growing Fe film (**Fig. 5a,c**), with thicker layers observed at the surface of Fe films grown from Fe_3O_4 as compared to Fe_2O_3. The gravimetric η_{Fe} was corrected for residual oxides using EPMA and was similar for both oxides; 80% for *np*-Fe_3O_4 and 75% for *np*-Fe_2O_3. Fe films produced from *np*-Fe_3O_4 exhibited larger crystalline domains of Fe metal (5 µm or greater) which were joined to form extended branches

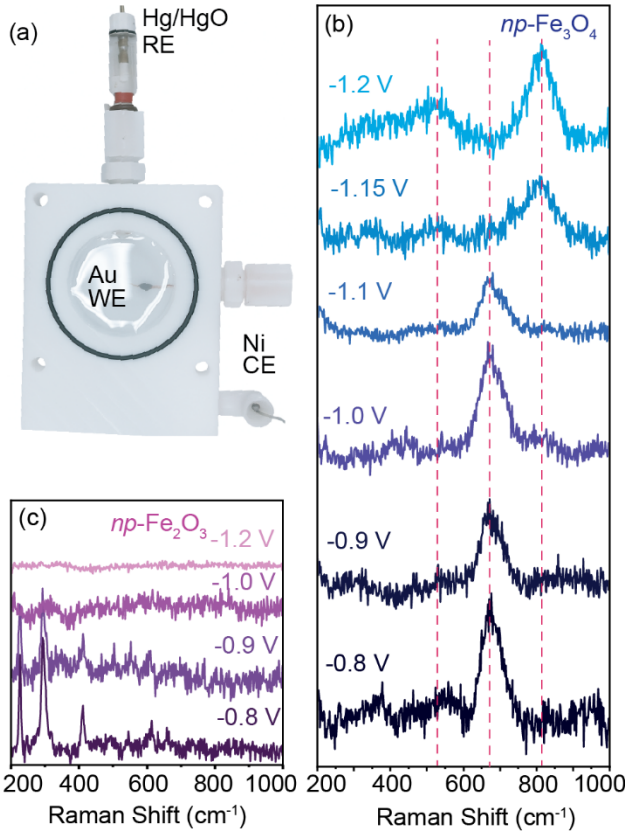

Figure 4: In-situ Raman of iron oxides. (a) Image of the immersion mode in-situ electrochemical Raman cell, with excitation provided by a 633 nm laser. In-situ Raman spectra of (b) *np*-Fe_3O_4 (c) *np*-Fe_2O_3 at different potentials. The experiments were performed at an elevated temperature of 60 °C. Dashed red lines in (b) are provided as guidelines and are at 538 cm^{-1}, 671 cm^{-1} and 815 cm^{-1}. A new feature was observed for Fe_3O_4 at negative potentials, but not for Fe_2O_3.

30 µm or more (**Fig. 5c, Fig. S22)**, whereas films growth from *np*-Fe_2O_3 generally exhibited smaller crystalline domains and more disordered branching (**Fig. 5a, Fig. S23)**.

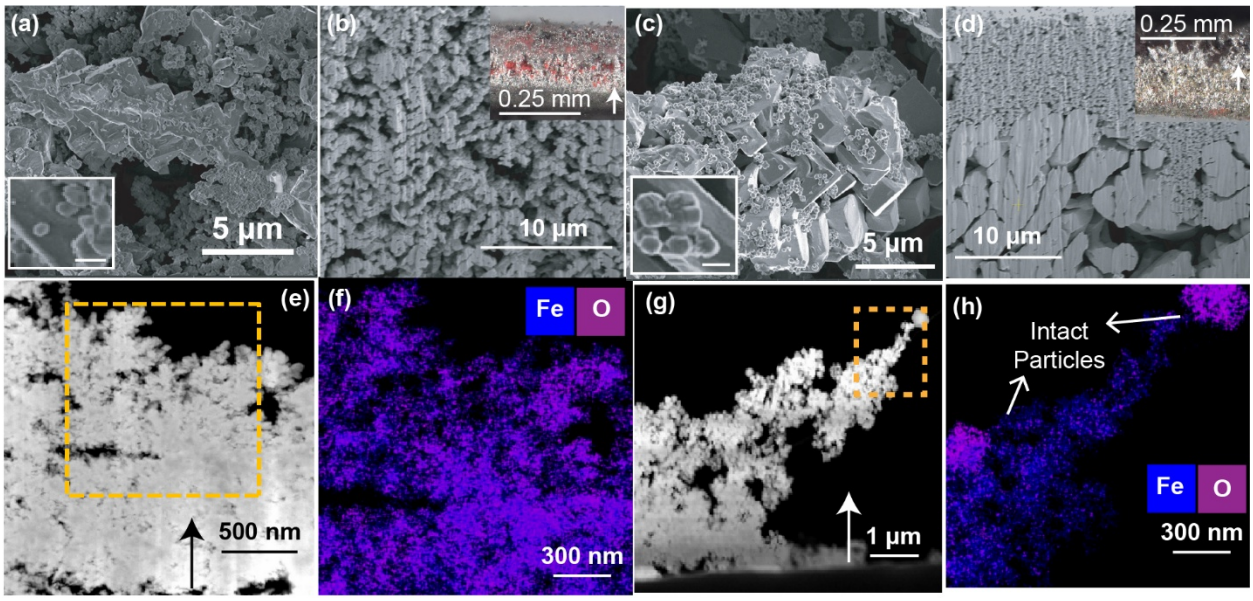

Figure 5: SEM and TEM characterization of Fe films. Secondary electron SEM images of iron films grown on Cu at −200 mA cm^{-2} for 1 h in 30% w/w NaOH at 82 °C from (a,b) *np*-Fe_2O_3, (c,d) *np*-Fe_3O_4 . Cross-sectional SEM image of the Fe-film prepared from (b) *np*-Fe_2O_3 and (d) *np*-Fe_3O_4 using a plasma FIB. (e, g) Fe films grown at −1.3 V vs Hg/HgO at 90 °C from (e) *np*-Fe_2O_3 or (g) *np*-Fe_3O_4. TEM-EDX mapping (f, h) of the dotted squares from e and g. Unreacted and partially reacted Fe_2O_3 and Fe_3O_4 particles are visible as lighter contrast regions on crystalline Fe in SEM images. The arrows in the inset optical images of (b, d, e, g) indicate the growth direction of the iron metal. The inset scale bars (a, c) represent 300 nm.

The internal morphology of porous Fe films was investigated with cross sections prepared using a focused ion beam (FIB) and monitored with SEM. These images revealed that Fe films prepared from *np*-Fe_3O_4 possessed larger grains and had less porosity compared to films prepared from *np*-Fe_2O_3 (**Fig. 5b,d**). The average grain size observed via FIB-SEM for *np*-Fe_2O_3 was < 3 µm, compared to > 10 µm for *np*-Fe_3O_4. **Figure 5e-h** show scanning transmission electron microscopy (TEM) images of Fe metal grown from *np*-Fe_3O_4 and *np*-Fe_2O_3 on an Au TEM grid, after reducing the iron oxides in 30% w/w NaOH at 90 °C at E = –1.3 V vs Hg/HgO. Both *np*-Fe_3O_4 and *np*-Fe_2O_3 were completely reduced to iron metal films based on selected area diffraction pattern (SAED) (**Fig. S24, S25**) and EDX analysis (**Fig. 5f,h**). Incipient Fe films exhibited similar

grain sizes of Fe metal (<100 nm), regardless of the reactant oxide (**Fig. 5e, g**). These grains were inconsistent with the micrometer size grains observed in the growth region of films produced during extended electrolysis (20–60 minutes). In some instances, Fe dendrites could be seen growing in the direction of intact *np*-Fe_3O_4 particles, consistent with a growth mechanism fed by soluble intermediates rather than a direct solid-state reduction mechanism.

Activating inactive Fe_3O_4 particles

To demonstrate the potential impact of nanoscale iron oxide conversions on large-scale ironmaking process, we developed a gram-scale reprecipitation-electrowinning method based on acids and bases with existing supplies >10^7 t/y to convert *bf*-Fe_3O_4 into nanoscale Fe_3O_4 precursors (**Figure 6a**, **Supporting Information)**. Dissolution of *bf*-Fe_3O_4 was accomplished in HCl(aq) and the Fe^{2+}/Fe^{3+} mixture was reprecipitated with the addition of NaOH(aq) followed by filtration to yield an iron-oxide sample (*prec*-Fe_3O_4) with a specific surface area (BET: 229 $m^2\ g^{-1}$) that was ~100x that of the original *bf*-Fe_3O_4 powder. The XRD pattern of the precipitate was consistent with a phase-pure Fe_3O_4 sample with nanoscale crystallinity (**Fig. S26**) and TEM analysis showed that the particles were less than 10 nm in diameter (**Fig. 6b**). Furthermore, the precipitate was relatively free of impurities except for Ca (0.2 at.%), as detectable via EDX, unlike the particles before reprecipitation (**Table S2**).

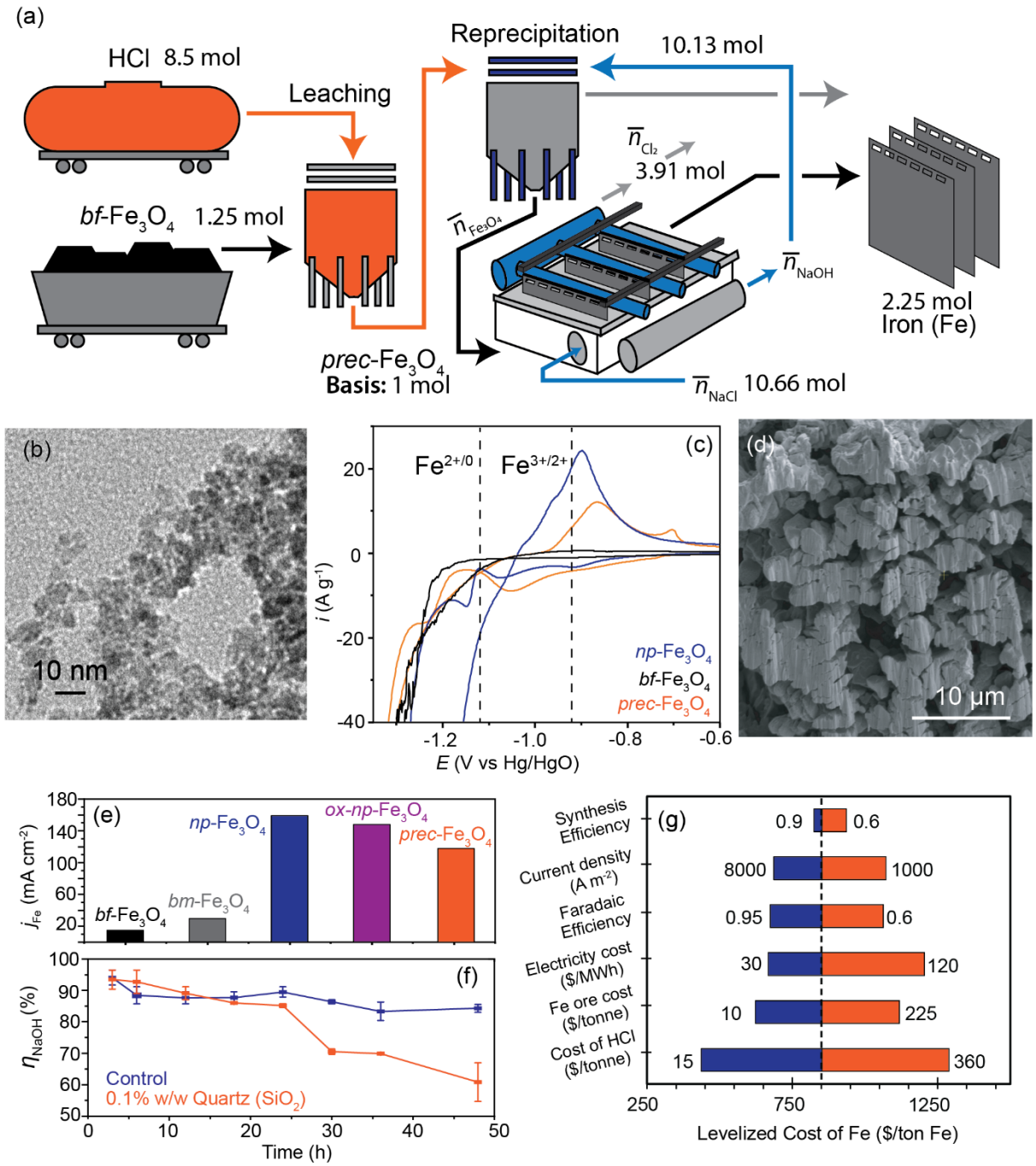

Figure 6: Reprecipitation of *bf*-Fe_3O_4 to synthesize *prec*-Fe_3O_4. (a) Simplified flow sheet for activating low surface area iron ores using chemical co-products from the chlor-iron process. (b) TEM image of the prec-Fe_3O_4. (c) CV of *prec*-Fe_3O_4 at multiple scan rates with a constant mass loading of 43 µg cm^{-2} in 30% w/w NaOH at 90 °C. (d) FIB-SEM cross-section of a metallic Fe film formed during bulk electrolysis. (e) Bar graph representing partial current density ($|j_{Fe}|$) of different iron oxide samples reduced at –200 mA cm^{-2} for 1 h. (f) Stability of NaOH current efficiency under exposure to soluble ore impurities in an accelerated stress test (90 °C and 500 mA/cm^2) (g) Technoeconomic analysis of the reprecipitation and electrowinning process. Assumed iron oxide synthesis efficiency (0.80), total current density (200 mA cm^{-2}), Faradaic efficiency (0.75), electricity cost ($61/MWh), Fe ore cost ($109.4/ton), and HCl cost ($183/ton) were used calculate the base-case. Reprecipitation of *bf*-Fe_3O_4 increased the rate of iron production.

Cyclic voltammetry of *prec*-Fe_3O_4 was qualitatively consistent with *np*-Fe_3O_4, rather than *bf*-Fe_3O_4. The onset of reduction current occurred at $E > -0.7$ V, and a prominent reduction peak occurred at $E = -1.05$ V. Another reduction wave that featured at $E = -1.25$ V did not yield a peak (**Fig. 6c**). Films of *prec*-Fe_3O_4 yielded the greatest gravimetric current density in the faradaic region assigned to $Fe^{3+/2+}$, but the onset to $Fe^{2+/0}$ current occurred at a more-negative potential compared to the other particles. Additionally, the thin-film RRDE of *prec*-Fe_3O_4 also yielded similar results (**Fig. S27**). A peak current was observed for *prec*-Fe_3O_4 at $E = -1.02$ V, whereas *bf*-Fe_3O_4 did not. A simultaneous current at the ring depicted a significant amount of aq. Fe^{2+} formed for *prec*-Fe_3O_4 and *bf*-Fe_3O_4 depicted no faradaic current in this region. *prec*-Fe_3O_4 exhibited another reduction wave onset at $E = -1.2$ V for $Fe^{2+/0}$ reduction, compared to *bf*-Fe_3O_4 which showed an onset at $E = -1.25$ V.

Impurities including Si and Ca were detected in *bf*-Fe_3O_4 at concentrations reaching up to 10% relative to the total Fe content. Subsequent reprecipitation of *bf*-Fe_3O_4 reduced the impurity level to 6%. To evaluate the influence of these impurities on electrochemical behavior, cyclic voltammetry of *np*-Fe_3O_4 was conducted in the presence of SiO_3^{2-} and Ca^{2+} and a progressive suppression of reductive currents was observed with increasing concentrations of both elements (**Fig. S28–S29**). While the presence of SiO_3^{2-} had negligible effect on the current response at potentials more positive than −1.15 V, even trace additions resulted in an approximately 50% attenuation of the peak current density at $E = -1.2$ V. In contrast, the introduction of 1 mM Ca^{2+} led to a sixfold reduction in peak current density at the same potential, indicating a more pronounced inhibitory effect relative to SiO_3^{2-}.

Bulk electrolysis of *bf*-Fe_3O_4 derived powders produced metallic Fe films at substantially greater η_{Fe} than direct electrolysis of the original particles. A cell biased at –200 mA cm^{-2}, yielded

a $|j_{Fe}|$ of 119 mA cm^{-2} (η_{Fe} = 59.5%). Electron probe microanalysis (EPMA) of the Fe film indicated less than 0.07% w/w for Si and 0.008% w/w Al impurities in the Fe film, indicating that either reprecipitation, filtration, and/or electrochemical reduction removed these impurities. A FIB-SEM cross-section of Fe film showed the size of the grain size to be < 10 μm (**Fig. 6d**) and EDX of the cross-section revealed the presence of 1% Ca in the film (**Table S2**). Further processing (ball-milling) to reduce the particle size of *bf*-Fe_3O_4 (*bm*-Fe_3O_4), yielded only a moderate increase to (η_{Fe} = 15%) (**Supporting information**).

Quantifying production of NaOH for precipitation

The cost of NaOH is generally too expensive ($500/$t_{NaOH}$) to support a reprecipitation process for ironmaking, but OH^- is a product of direct oxide reduction in alkaline electrolytes. We demonstrated the coproduction of NaOH and Fe using a recirculating chlor-iron cell, with a DSA electrode (De Nora Tech) evolving Cl_2 from 30% w/w NaCl and a bilayer N966 membrane (Chemours) designed for chlor-alkali cells separating the catholyte from the anolyte. Membranes were tested under a typical Na^+ flux for their design specification. Changes to [NaOH] in the catholyte were measured both by changes in density and titrations and used as to estimate the current efficiency towards NaOH (η_{NaOH}) over time. Compared to η_{NaOH} in stock 30% w/w NaOH, the η_{NaOH} in the presence of 25% w/w *bf*-Fe_3O_4 was lower but remained >85% for 1 h of continuous production (**Fig. S30**).

A 48 h accelerated stress test was performed in a recirculating cell to study the effect of quartz (SiO_2) as a simulated gangue impurity which could accumulate in the catholyte. Fe was not present in the catholyte for extended testing to eliminate the need for periodic collection of metal. In the presence of 0.1% w/w SiO_2 in the catholyte, the η_{NaOH} decreased from 94% at 3 h to 85% at

24 h. Then a greater reduction in η_{NaOH} was observed over the next 24 h, where it decreased to 61%. Impurities commonly found in iron ores could impact the production of NaOH and this motivates studies on the interaction of these species with ion-conducting membranes.

Technoeconomic analysis of Fe metal production from Fe_3O_4

A technoeconomic analysis of the reprecipitation-electrowinning method (**Fig. 6a**) integrated with a chlor-iron process capable of producing both Fe and NaOH(aq) from iron oxides and NaCl(aq). We explored how the quantity and cost of HCl used for Fe_3O_4 dissolution influence the overall economics of the ironmaking process (**Fig. 6f**). Cost estimates for the stack and balance-of-plant (BOP) were derived from published data on chlor-alkali and metal-electrowinning processes and are summarized in the Supporting Information (**Tables S3-S4**).[24,36,37] The levelized cost of iron, X_{Fe}, was calculated based on estimated capital costs for and operating costs and an annual revenue for co-sale of Cl_2 at \$250/t (**Equation 4**, Supporting Information)

$$X_{\mathrm{Fe}} = \sum_y \left[\frac{C_i - R_{Cl2}}{(1+r)^y}\right] / \sum_y \left[\frac{P}{(1+r)^y}\right] \quad (4)$$

where, C_i represents the area specific cost of the raw materials and manufacturing, y is the model year, r is the discount rate (0.08), P is the tonnes of iron product, and R_{Cl_2} is the revenue generated from co-sale of Cl_2. Assuming co-sale of Cl_2 and levelizing the cost of Fe against the remaining project costs leads to a X_{Fe} which is highly sensitive to the assumed chlorine price. We have used \$250/t as a conservative estimate for the U.S. base case (prices in North America have remained >\$500/t since 2024) and hold this fixed for all other modeling cases to highlight the impact of other modeling parameters.

The cost and amount of HCl used for the reprecipitation dominate the overall cost of Fe electrowinning (**Figure 6f**). By comparison, the effects of improved synthesis efficiency, reduced

Fe ore costs, and/or reduced electricity consumption are marginal in their impact on the total cost of production of Fe. The levelized cost of 1.0 t of Fe was estimated to be $\$851/t_{Fe}$ considering a moderate cost for acid ($\$183/t_{HCl}$) with 0.50 mol excess the stoichiometric amount of HCl required to dissolve Fe_3O_4 (**Equation 7**). In China, where HCl costs are as low as ($\$13/t_{HCl}$), the levelized cost of Fe could be as low as $\$491/t_{Fe}$, which is competitive with regional prices for iron produced in direct reduced iron (DRI) furnaces. However, in regions with high costs of HCl and electricity such as Brazil, the X_{Fe} is much greater ($1,231, **Table 1**).[38] The indirect carbon emissions resulting from electric power supplied to the cell are sensitive to the energy efficiency of the process and the electricity mix. We estimate indirect emissions from 0.20–3.06 t_{CO2}/t_{Fe} with the lowest carbon intensity occurring in Norway.

Table 1: Variation in levelized cost of Fe (X_{Fe}) for a few representative pricing scenarios with varying costs associated for HCl(aq) and industrial power.[39–42] Electrical costs ($/MWh) were estimated based on reported industrial electricity prices in the specified states and countries in 2024 and costs of HCl were representative based on trends in prices over 2020–2024. References provided in the Supplementary Information.

Country (Region)	P_{HCl} ($/t)	P_{power} ($/MWh)	X_{Fe} ($/$t_{Fe}$)	t_{CO2}/t_{Fe}
Norway (Europe)	152	37	632	0.20
China (N.E. Asia)	15	71	491	3.06
Brazil (S. America)	230	130	1,231	0.54
United States (Texas)	183	61	851	2.23
United States (Washington)	183	66	881	0.67

The capital cost of the electrowinning stack was estimated assuming area-specific cell costs consistent with chlor-alkali stacks and j_{tot} consistent with the experiments performed here (200 mA cm^{-2}). Further increases in the operating current density has a minor impact on X_{Fe}, but reducing $|j_{Fe}|$ to levels consistent with electrowinning of dissolved Cu or Zn (< 75 mA cm^{-2}) could increase

the X_{Fe} considerably. We assumed a η_{Fe} which is closer to the η_{Fe} observed for *np*-Fe_3O_4 (0.80) than that observed for *prec*-Fe_3O_4 (0.60). This assumption rests on continued improvement of this early-stage process and models where η_{Fe} remains at 0.60 lead to X_{Fe} = \$1063/t_{Fe}, an increase of ~\$200/t_{Fe} compared to the base case. Substantial Faradaic efficiency improvements (0.95) are required to further reduce X_{Fe} <\$700 (**Fig. 6f**).

Discussion:

Relationship between nanoscale particles, soluble Fe^{2+}, and the faradaic efficiency (η_{Fe})

Thin-film voltammetry of iron oxide particles revealed that the rate of soluble Fe^{2+} production is a potential descriptor for the activity of iron oxides for bulk Fe production in alkaline electrolytes. Films prepared from *pc*-Fe_2O_3 yielded both the greatest $\eta_{Fe^{2+}}$ and η_{Fe}, followed by *an*-Fe_2O_3 and *bf*-Fe_3O_4, and this trend was reflected in the thickness of Fe film prepared during electrowinning (**Fig. 1c-e**). Although *an*-Fe_2O_3 showed a sharp peak in the ring current, indicating some formation of soluble Fe^{2+}, the maximum $\eta_{Fe^{2+}}$ was small (3%) compared to *pc*-Fe_2O_3 (36%) and *bf*-Fe_3O_4 did not show any sign of soluble Fe^{2+} (**Fig. 1b**). Collectively, these results suggest that particles exhibiting a high gravimetric surface area can support rapid formation of soluble Fe^{2+} species and that these intermediates are a precursor to high specific current densities towards iron metal in alkaline electrolytes. These results correlated strongly with the η_{Fe} in the batch cell, suggesting that the kinetic competition between H_2 evolution and Fe growth may be controlled by the rate of Fe^{2+} generation at the surface. However, other factors such as adsorbed impurities, evolving electronic conductivity of the porous Fe films, adsorbed gas bubbles, and transport within porous deposits will also play a role in determining η_{Fe}.

Morphology plays a similarly important role during high-temperature reduction of iron oxide pellets by H_2 and NH_3 gas, where the gas phase transport of reactant H_2 and product H_2O is necessary.[11,12,43] However, soluble Fe^{2+} intermediates can participate in reprecipitation reactions with iron oxides and intermediates present in the reactive layer, prior to collection at growing Fe metal domains, posing unique challenges for low temperature, aqueous reduction.

Effect of metal oxide phase on the mechanism of iron-oxide reduction

Despite its purported role as a reaction intermediate, several studies have reported Fe_3O_4 to be less active than α-Fe_2O_3 during electrochemical reduction in concentrated alkali.[44,45] While aggregates of α-Fe_2O_3 nanoparticles (BET surface area 13 $m^2\ g^{-1}$) support absolute partial current densities towards Fe metal ($|j_{Fe}|$) in excess of 500 mA cm^{-2}, commercial Fe_3O_4 suspensions lead to lesser $|j_{Fe}|$ values (<30 mA cm^{-2}).[46,47] Only sintered Fe_3O_4 films, with micron-scale porosity (45.5% pore volume) have exhibited $|j_{Fe}| > 100$ mA cm^{-2}, hinting at the importance of reactant morphology.[48] Morphology has a substantial influence on the reaction mechanism of hematite reduction,[24,29] and here, well-defined particles of α-Fe_2O_3 and Fe_3O_4 were prepared to study the intrinsic differences between iron-oxide phases undergoing conversion at low temperatures. α-Fe_2O_3 was synthesized directly from Fe_3O_4 nanoparticles (*np*-Fe_2O_3) to ensure that differences in particle size did not contribute to differences in reactivity. This *np*-Fe_2O_3 behaved similarly to high-surface-area hematite aggregates, *pc*-Fe_2O_3 (**Fig. 1a, 2a, 3d**), whereas the electrochemical behavior of *np*-Fe_3O_4 was altogether different from either *np*-Fe_2O_3 or *pc*-Fe_2O_3 (**Fig. 2a,b**), suggesting that the phase of the reactant oxide influences the collection of soluble intermediates. Moreover, scan-rate dependent CVs revealed an unexpected increase in the extent of reaction for *np*-Fe_3O_4 with increasing scan-rates, while *np*-Fe_2O_3 yielded a scan-rate dependence consistent with a kinetically limited reductive dissolution process (**Fig. S11**). At 500 mV/s, more cathodic charge is passed

during *np*-Fe_3O_4 (2.0 mC, 18.5%) reduction compared to *np*-Fe_2O_3 (1.29 mC, 11.9%). Similar trends were observed during reduction under forced convection at an RRDE (**Fig. 3**). Morphologically similar Fe_2O_3 and Fe_3O_4 show different electrochemical reduction behaviors.

The lesser rate of soluble Fe^{2+} collection from thin films of *np*-Fe_3O_4 could result from a few physical differences between Fe_3O_4 and α-Fe_2O_3 particles: (1) reduced kinetics towards reductive dissolution for Fe_3O_4 compared to α-Fe_2O_3 due to a lesser fraction of surface Fe^{3+} sites, (2) inhibited O^{2-} or OH^- transport to the reacting surface layer, leading to passivation, or (3) chemical reactions at the Fe_3O_4 surface which do not occur at the Fe_2O_3 surface. The first and second possibilities are inconsistent with the increase in cathodic charge with increasing scan rate, suggesting that a potential-independent chemical reaction could be related to lower rates of Fe^{2+} formation. This reaction could be driven by soluble Fe^{2+} generated at particle interface or kinetically limited phase transition caused by an excess of Fe- or O-vacancies at the reduced Fe_3O_4 surface.

In-situ Raman spectroscopy identified metal-oxide phases formed during conversion of *np*-Fe_3O_4 films under potentiostatic control in NaOH(aq) at 60 °C. The Raman peaks assigned to Fe_3O_4 vanished at -1.15 V, similar to the potentials where Fe^{2+} collection was diminished at the RRDE, and these peaks were replaced by two new peaks at 538 cm^{-1} and 815 cm^{-1}. We speculate that these peaks should be assigned to a new (hydr)oxide layer on Fe_3O_4 during conversion of magnetite in NaOH (**Fig. 4b, Fig. S18**). These features were observed only under cathodic bias at –1.2 V, where metallic iron is formed from both *np*-Fe_3O_4 and *np*-Fe_2O_3, consistent with electrochemical passivity (**Fig. 2c, 3a**). A thorough review of the Raman peaks measured in air for common iron oxides and oxy/hydroxides failed to yield matching peaks at 538 cm^{-1} and 815 cm^{-1} (**Table S5-S6**). The lower energy peak could be compared against hematite and goethite (α-FeOOH) which exhibit peaks assigned to Fe–O stretching at 498 cm^{-1} and 550 cm^{-1},

respectively.[49,50] Hematite also exhibits a peak assigned to two-magnon scattering, which occurs only in antiferromagnetic materials, at 820 cm^{-1}, but other characteristic peaks associated with the material were absent.[49] Both peaks were only observed under cathodic bias and a peak at 670 cm^{-1}, attributable to Fe_3O_4, re-emerged within minutes of the potential returning to $E > -1.0$ V. Ex-situ TEM characterization of Fe_3O_4 upon reducing at –1.1 V, depicted an amorphous layer of ~3-4 nm around the particle, consistent with the hypothesis of a passivating layer (**Fig. S21**). Moreover, the interior of the particle was still crystalline Fe_3O_4, suggesting that this layer could inhibit further conversion of the particle. Previous studies in neutral aqueous environments have also observed surface passivation of Fe_3O_4 in the presence of soluble Fe^{2+} species, where this process occurs via Fe atom exchange.[51,52] RRDE studies at varied temperature and [NaOH], where either increasing the temperature to 110 °C or the [NaOH] to 50% w/w increased the rate of Fe^{2+} collection (**Fig. S13-S15**), indicate that modified cell conditions can assist in activating iron oxides with slow dissolution kinetics. Limits to the operating temperature and [NaOH] are primarily imposed by the cation exchange membrane, with reprecipitation becoming uneconomical when NaOH is not a co-product of the ironmaking process. Because the layer identified in Raman and *ex-situ* TEM was not matched to a specific phase or composition, conclusive evidence supporting a passivation mechanism is lacking. Further *in-situ* characterization is necessary to determine if passivation is indeed the cause of anomalously low reactivity of Fe_3O_4 particles towards Fe^{2+} production.

Similar Raman features were not observed in spectra of *np*-Fe_2O_3 during reduction (**Fig. 4c**), which is correlated with trends in the ring current during reduction of *np*-Fe_2O_3 (**Fig. 3e**). However, Fe films produced from *np*-Fe_2O_3 and then oxidized at –0.3 V did yield a Raman peak at 671 cm^{-1}, indicating that previously reported Fe_3O_4 phases may result from oxidation of high-surface-area Fe rather than serving as an intermediate phase during Fe_2O_3 reduction. As with Fe_3O_4

intermediates, careful consideration of the environmental history of Fe films is required when interpreting XRD and TEM data.[29,32,53] Formation of fully oxidized phases such as γ-Fe_2O_3 could be driven by chemical reactions with O_2, which is expected to be facile due to the similar cubic structure of both the phases.

Metallic Fe film formation from *np*-Fe_3O_4 and *np*-Fe_2O_3 at –200 mA cm^{-2} produced comparable Fe deposition efficiencies (η_{Fe}), with a η_{Fe} approaching 80% both samples. The maximum $\eta_{Fe^{2+}}$ values of 80% for *np*-Fe_3O_4 and 100% for *np*-Fe_2O_3 were obtained at a scan rate of 10 mV s^{-1} (**Fig. 3c, f**). Although the reduction peak current in *np*-Fe_3O_4 was three times lower than *np*-Fe_2O_3 (**Fig. 2c, d and Fig. 3a, d**), a clear correlation between $\eta_{Fe^{2+}}$ and η_{Fe} was established. These findings suggest that the CV peak height alone is insufficient to assess the activity of iron oxides toward metallic Fe formation, instead, $\eta_{Fe^{2+}}$ serves as a more meaningful indicator.

Fe films grown from *np*-Fe_3O_4 and *np*-Fe_2O_3 exhibit differences in micron-scale grain structure. Nucleation dominates the Fe deposition process during the early stage of film growth and STEM images of the Fe films deposited from *np*-Fe_3O_4 and *np*-Fe_2O_3 showed the presence of nanoscale Fe metal domains adjacent to unreacted oxide particles (**Fig. 5**). At later stages of film growth, micron-scale Fe grains produced from *np*-Fe_3O_4 were 2-3 times larger than those of *np*-Fe_2O_3 (**Fig. 5**). Additionally, FIB-SEM images revealed that the Fe film prepared from *np*-Fe_2O_3 were more porous (**Fig. 5b, d**) and Fe branches produced from *np*-Fe_3O_4 continue to grow to

crystals of 15-20 μm. Differences in the grain size and rate of nucleation could be related to differences in the surface activity of soluble ferrous species resulting from the distinct oxide phases.

Reprecipitation enables the production of Fe at high rates from previously inactive iron oxides

Coupled thin-film RRDE and CV results suggest that iron oxides producing a higher $\eta_{Fe^{2+}}$ also exhibit higher η_{Fe} during batch-cell electrolysis (**Fig. 3c,f, 6e**). One possible explanation for why blast furnace powders (*bf*-Fe_3O_4) are less active than high-surface-area Fe_2O_3 powders during electrochemical ironmaking is that a lower rate of Fe^{2+} generation the lower specific surface area relative to recently precipitated Fe_2O_3 powders (**Fig. 1b,f**). Modifying the morphology of the *bf*-Fe_3O_4 using a precipitation and filtration route tested this specific-surface-area hypothesis (**Supporting Information**). Processed *bf*-Fe_3O_4 yielded *prec*-Fe_3O_4 with a high BET surface area (229.2 $m^2\ g^{-1}$) and a small particle diameter < 10 nm (**Fig. 6b**) and these changes to the morphology led to increased gravimetric activity during thin film voltammetry and also increased η_{Fe} during electrolysis at –200 mA cm^{-2} (**Fig. 6c, e**). These results indicate that any intrinsic differences in dissolution between Fe_2O_3 and Fe_3O_4 may be surpassed by preparing high-surface-area powders.

Batch cell electrolysis of impurity-free nanoparticles of Fe_3O_4 and Fe_2O_3 yielded an average η_{Fe} of 80% and $|j_{Fe}|$ of 160 mA cm^{-2} (**Fig. 6e**), suggesting that nanoscale Fe_3O_4 and Fe_2O_3 particles exhibit similar reactivity during alkaline electrowinning. Although *prec*-Fe_3O_4 yielded $|j_{Fe}|$ of 119 mA cm^{-2}, nine times higher than that obtained from *bf*-Fe_3O_4 (14 mA cm^{-2}, **Fig. 6e**), trace Ca^{2+} or Si^{4+} impurities may have influenced the kinetics of iron reduction or water reduction. One of the highest $|j_{Fe}|$ for magnetite reported to date (115.5 mA cm^{-2}) was obtained from a Fe_3O_4 pellet possessing large macropores and high specific surface area, which have some similarities to the reactive layers observed via SEM (**Fig. 5d**).[48] Studies employing suspensions of Fe_3O_4 particles

have generally reported much lower $|j_{Fe}|$ (e.g. < 30 mA cm^{-2}), whereas the blast-furnace particles, which are impurity-rich and morphologically ill-defined Fe_3O_4 achieved higher $|j_{Fe}|$ than even commercially available Fe_3O_4, a result which we attribute mainly to the differences in tendency of the particles to form a porous, high-surface-area film on the growing metal surface.[22,25,45] Similar approaches to dissolving taconite and Fe waste streams in HCl to yield $FeCl_2$ have been used to prepare molten-salt electrolytes which can be reduced at 500 °C to obtain metallic Fe at η > 85%.[17,19]

The morphology of Fe films prepared from *prec*-Fe_3O_4 differed significantly from those produced from *np*-Fe_3O_4 and *np*-Fe_2O_3 as observed in the cross-sectional SEM images (**Fig. 5a-d, Fig. 6c**). This difference in morphology could result from either different impurities or differences in j_{Fe}. EDX of *prec*-Fe_3O_4 sample showed 0.2 at.% of Ca (**Table S2**), while the EDX of the Fe film exhibited 0.1 at.% of Si and 0.3 at.% of Ca (**Table S2**), which is consistent with adsorbates or thin film of precipitates. Precipitated Si and Ca (hydr)oxides at electrode surfaces have previously been shown to inhibit charge transfer reactions.[54,55] Trace quantities of dissolved Si- and Ca-containing species can substantially affect the local deposition current (**Fig. S28, S29**). A reduced $|j_{Fe}|$ is likely accompanied by greater $|j_{H_2}|$ and the generation of gas bubbles within the film also impacts the morphology. Increased surface area of Fe films produced during electrowinning have a complex relationship with j_{Fe} relative to the total current.[23]

Gangue elements will be incorporated into electrodeposited Fe in different quantities and compounds compared to direct reduced iron. Small quantities of impurities can thus significantly alter the morphology of the Fe films produced via alkaline electrowinning, either by adsorbing or precipitating on the metal surface or modifying the rate of formation for soluble Fe^{2+} intermediates or the deposition rate. The amount of Si in the electrodeposited Fe film (0.3 at.%), was less than a

typical Si content for DRI (3 at.%) but Ca was incorporated in a greater amount (2.7 at.%) compared to DRI (0.66 at.%) (**Table S2**).[56] These impurities can be removed with slag formed in electric arc furnaces, but a large quantity of Ca could require changes to melting procedures. Amphoteric impurities such as Si and Al that are soluble in strong base will be more readily separated from the iron product whereas insoluble Ca and Mg will require removal in downstream steps.

Analysis of reprecipitation for ironmaking at scale

A technoeconomic analysis of the reprecipitation process in chlor-iron plant reveals that the cost of chemicals (HCl) for extracting Fe from ores is the most significant factor on the final cost of Fe metal (**Fig. 6f, Table S3-S4, Fig. S31-32**). This means that if reprecipitation is accomplished with concentrated acids produced in a separate process, the approach will only be favorable in regions with excess acid production. Presently, the use of HCl as a reagent is most cost-effective in China but the electric power costs and carbon intensity are minimized when the process is conducted on a grid similar to Norway (**Table 1**). Because purchase of NaOH is not expected to be economical, maintaining $\eta_{NaOH} > \eta_{Fe}$ is necessary to ensure that waste streams generated by the process remain pH neutral or mildly alkaline (**Fig. S32**).

Because Cl_2 is a co-product of NaOH production, which can be combined with the alkaline ironmaking step, a process to generate HCl directly from Cl_2 could further reduce the levelized cost of Fe and lead to a fully integrated chlor-iron process for activating iron oxides towards electrochemical ironmaking (**Figure 6a)**. On-site utilization of Cl_2 could minimize the energy required for storage, compression and transport of Cl_2 but would increase the balance of plant costs due to additional reactors required for HCl generation. This method of processing ore is unproven and the assumptions underlying the chemical looping configuration will require substantial effort for

development. Economic viability depends on integration with regional chemical markets, including inexpensive access to HCl and the productive use or sale of Cl_2.

Existing and alternate pathways for producing iron and steel

The integrated process for electrochemical ironmaking proposed here is distinct in both its challenges and advantages compared to existing processes. Iron ores can be reduced to metal using natural gas or carbon-free reductants (e.g. hydrogen, ammonia) in the direct reduced iron process (DRI). These methods are routinely practiced at the million ton per year (MMTa) scale and are much more mature than electrochemical ironmaking.[11,13,43] The costs associated with an integrated DRI furnace and electric arc furnace was recently estimated at $582 per tonne of steel and while the overall process leads to 1.32 tonnes of CO_2 per tonne of steel, 0.55 tonnes are associated with the DRI furnace.[57] The latter emissions are what are targeted by an electrified ironmaking process. The DRI process is robust and requires relatively inexpensive maintenance and consumables (e.g. periodic replacement of reformer catalysts) estimated in the range of \$1–10 x 10^6 per year,[57] whereas the 300,000 tonne chlor-iron system modeled here assumes a stack replacement (\$3 x 10^8) every 6 years and more frequent required replacement of the anodes or membranes within the stacks could add additional maintenance costs in the range of \$10 x 10^6. Since gangue impurities will likely impact maintenance costs, the design of membranes and anodes which are tolerant to the unique set of impurities introduced by an iron electrowinning environment is necessary to improve the competitiveness of this approach. This is an unresolved challenge and longer durability experiments (>100 h) studying the impact of realistic gangue impurities during simultaneous ironmaking are needed to provide clarity on these costs.

One alternative process which is at a significantly greater stage of technological readiness involves production of H_2 and iron in separate steps, which benefits from similarity in design to

the existing DRI process. When H_2 is generated electrochemically, this avoids the majority of direct emissions, eliminates the reforming step, and offers longer expected lifetimes for electrochemical stacks.[58] However, this approach requires H_2 costs < \$1.7 kg^{-1} for cost parity with the incumbent systems powered by gas at \$33.85 MWh^{-1} and if electrochemical steps are driven by intermittent electricity, storage of H_2 will likely be more expensive compared to storing iron.[57,59] The total energy requirement and system cost will increase when using alternative fuels as H_2 carriers, which must offset the additional costs by producing hydrogen in regions with more plentiful electricity. A fundamental challenge faced by direct reduction is the fact that gangue impurities are trapped within the iron product. Low-temperature direct reduction, when facilitated by dissolved intermediates, can extract Fe from gangue impurities and is thus more tolerant to a wider range of feedstocks.

Acidic electrowinning also relies on dissolved intermediates and can benefit from an even wider range of feedstocks. Selective oxygen evolving anodes in acidic electrolytes recover the H^+ necessary for dissolution, thereby avoiding sensitivities to chemical costs of dissolution.[16] Electrolytic iron is an existing product used in specialty steelmaking today, when exceptional purity is required.[60] The primary drawbacks of iron production from iron dissolved in aqueous electrolytes is that the areal productivity of the cells are expected to be lower in comparison to cells directly reducing iron oxide solids (**Fig. 6g**). Molten chloride and molten oxide electrolysis enable higher current densities than either approach to low temperature electrolysis; aluminum smelting relies on a molten salt electrolyte and many smelters produce >0.5 million tonnes per annum (MMTa) which is equivalent to ~1 MMTa Fe on a mole basis.[18,19] We estimate that a 0.3 million MMTa plant (appropriate for supporting a 1 MMTa electric arc furnace fed primarily by scrap and similar

in Cl_2/NaOH production to a large chlor-alkali plant) would require a tank house with 308 cells, with a footprint of 770 m^2, and consume 215 MW of electricity (**Supplementary Information**).

The avoided emissions resulting from electrochemical ironmaking processes depends largely on the indirect CO_2 emissions associated with the high electricity demand, which is determined by the cell voltage, the oxidation state of the iron feedstock, and the carbon intensity of the grid. Direct reduction of Fe_3O_4 offers an 11% reduction in the energy required to produce Fe relative to iron(III) oxides such as Fe_2O_3. High cell voltages and/or low Faradaic efficiencies towards Fe would require direct integration with clean electricity to offer lower CO_2 emissions than DRI furnaces. The grid mix in 2024 Norway was clean enough for a ~0.35 t_{CO2}/t_{Fe} reduction in emissions compared to a natural gas DRI furnace, but most other grids produced too much CO_2 per MWh for the process to offer an emissions advantage. Continued expansion of wind, solar, and nuclear power capacity would lead to expanded regions where electrified ironmaking offers an emissions advantage over DRI furnaces.

Conclusion:

The electrochemical production of Fe from iron oxides at low temperatures is controlled by the nanoscale morphology of the precursor and its phase. The variation in electrochemical behavior of homologous α-Fe_2O_3 and Fe_3O_4 particles indicates that each iron oxide proceeds through a distinct reduction pathway, as also evidenced by the morphology of the Fe metal produced from different phases of iron oxide. Both Fe_3O_4 and α-Fe_2O_3 follow a reductive dissolution pathway in which soluble Fe^{2+} is produced during reduction prior to the formation of metallic Fe. *In-situ* electrochemical measurements of Fe^{2+} and spectroscopy of the oxide surface support a hypothesis that Fe_3O_4 particles passivate during reduction; this behavior was not observed with similarly sized α-

Fe_2O_3 particles. The rate of Fe^{2+} formation during thin-film voltammetry is generally correlated with the faradaic efficiency of Fe production in an electrowinning cell, and high-surface-area films of Fe_3O_4 and α-Fe_2O_3 yielded similar faradaic efficiency at –200 mA cm^{-2}. Careful control of particle morphology can thus overcome intrinsic reactivity differences associated with the reactant iron oxide phase. Differences in reactivity between Fe_3O_4 and Fe_2O_3 do not appear to limit Fe metal formation from <100 nm particles converted at high rates, possibly because consumption of dissolved Fe^{2+} prevents passivation of nanoscale magnetite domains. Further *in-situ* characterization is necessary to understand whether surface layers reported here for Fe_3O_4 are a cause or effect of lower rates of Fe^{2+} generation.

An integrated reprecipitation-electrowinning process fed by Fe_3O_4-rich ores enabled Fe metal formation with a ninefold greater η_{Fe} (59.5%) in comparison to the unprocessed powder and a j_{Fe} (–119 mA cm^{-2}) among the highest reported values from a Fe_3O_4 reactant. When low-cost acid is available, this addresses a key pitfall of alkaline iron oxide electrowinning, namely that most experimental demonstrations have employed high-purity Fe_2O_3 powders which are uneconomical as reagents for commodity ironmaking. However, durable membranes and anodes in the presence of ore impurities remain unsolved technical challenges for chlor-iron cells. Ultimately, low-cost and low-carbon electricity combined with a chlor-iron process integrated with recovery of HCl from co-product Cl_2 could enable scalable ironmaking with minimal carbon emissions.

Experimental Methods:

Materials: Deionized water (DI H_2O) with a resistivity of ≥18.1 MΩ·cm was taken from a Millipore deionization system. Ferrous nitrate hexahydrate ($Fe(NO_3)_2 \cdot 6H_2O$, 97%) and sodium hydroxide (NaOH, 50% w/w) were procured from Thermo Scientific and Fisher Chemical, respectively. A blast-furnace-grade iron ore concentrate served as a representative iron feedstock. Nickel

wire (600 Ni, Malin Co.) was used as the counter electrode, and a Hg/HgO reference electrode (CH Instruments) was calibrated in 30 % w/w NaOH and measured to be 0.930 V vs. RHE at 90 °C. Ball milling was performed in an Across International Planetary Ball Mill using alumina beads.

Electrochemical measurements: A Biologic SP-200 potentiostat was used to collect electrochemical data. A 50 mL polytetrafluoroethylene (PTFE) cell was used as the electrochemical reactor. NaOH electrolytes were prepared by diluting 50 % w/w NaOH stock solutions to 30 % w/w with DI H_2O and purged with N_2 for at least 30 min prior to experiments.

Thin films of iron oxides were prepared by drop-casting 2–3 μL of a 1 mg mL^{-1} particle suspension in DI H_2O onto glassy carbon working electrodes, followed by drying under an IR lamp. The suspensions were dispersed using horn sonication (SX Ultrasonics) and redispersed in a bath sonicator before casting. Electrodes for TEM were prepared by drop-casting 2 μL of the same suspension onto Au TEM grids (Ted Pella) and drying under an IR lamp.

A glassy carbon ring-disk electrode was used for RRDE measurements, with a disk radius of 3 mm and inner/outer ring radii of 4 and 5 mm, respectively. The RRDE system was controlled by a BlueRev RC-10k (BioLogic). The mass loading of iron oxides was 43 μg cm^{-2}, drop-cast onto the disk of the electrode. The disk was swept at 5 mV/s while keeping the ring fixed at the potential (–0.3 V vs Hg/HgO) to collect soluble Fe^{2+} produced at the disk during reduction.

Bulk electrolysis of iron oxide powders was performed in a horizontal three-electrode cell setup with a polished Cu foil serving as the working electrode, Ni foils as the counter electrode and Hg/HgO as the reference electrode. A suspension of 25% w/w iron oxide was prepared by suspending 6 g of iron oxide in 15 mL of 30 w/w % NaOH. Bulk electrolyses were performed for 20-60 min at –200 mA cm^{-2} with the cell temperature maintained at 82 °C. After electrolysis, the

Cu sheet was washed thoroughly with DI water and dried under an IR lamp. The gravimetric faradaic efficiency was calculated by measuring the weight of the Cu sheet before and after electrolysis and was corrected for oxide content. Electron probe micro analyzer (EPMA) measurements were conducted on a CAMECA SX100 Electron Microprobe to quantify the amount of metallic Fe versus the adsorbed and unreacted form of Fe (**Equation 5**)

$$\eta_{\mathrm{Fe}} = \frac{n\mathrm{F}m_{\mathrm{Fe}}f}{M_{\mathrm{r}}j_{\mathrm{tot}}t^{*}} \times 100 \qquad (5)$$

where, n is the number of electrons per Fe atom, F is the Faraday constant, m_{Fe} is the Fe-film mass, f is the mass fraction of Fe metal calculated using EPMA, M_{Fe} is the molar mass of Fe, j_{tot} is the applied current density and t^{*} is the electrolysis time.

NaOH production in a chlor-iron environment was evaluated using a cation exchange membrane (CEM, Nafion N966) positioned between identical geometric areas (2 cm × 7 cm) of a Ni mesh cathode and a RuOx/Ti anode in a zero-gap electrochemical cell operated with recirculating catholyte and anolyte streams. Before performance evaluation, the CEM was preconditioned for 1 h under zero-current conditions using recirculated electrolyte solutions. A 3-L anolyte reservoir contained 30% w/w of NaCl, while the 3-L catholyte reservoir contained 30% w/w of NaOH with additional solids added in some experiments to simulate a chlor-iron environment. The simultaneous production of Fe and NaOH was evaluated over 1 h using a 25% w/w suspension of *bf*-Fe_3O_4 whereas the long-term stability of the cell was evaluated with a suspension of 0.1% w/w of quartz (SiO_2) solids to simulate accumulated gangue impurities. Long term stability was not evaluated along with Fe growth because the membrane test fixture was not optimized for Fe collection. The cell temperature was maintained at 90 °C using a silicone heating pad (Omega Engineering). During the stability test, catholyte samples were periodically collected, cooled to room temperature,

and the NaOH current efficiency (η_{NaOH}) was monitored by changes in density after removal of solids via centrifugation.

Materials Characterization: Powder X-ray diffraction (XRD) patterns of the iron oxide powders were recorded on a Bruker D2 Phaser using a Cu Kα radiation source (λ = 1.54 Å), with a step size of 0.02° and a 2θ scan range of 15–70°. Raman spectra were acquired using a Renishaw Raman microscope equipped with a 633 nm red laser (0.1 mW) as the excitation source and averaged over five acquisitions. Microstructural analysis was performed using a Thermo Scientific Apreo 2 scanning electron microscope (SEM) operated at 5–15 keV. Transmission electron microscopy (TEM) was conducted on a FEI Titan microscope operating at 80 kV. Optical images were collected from the Keyence optical microscope.

In-situ Raman spectroscopy was performed in immersion mode in a custom electrochemical cell machined out of PTFE. A 50x objective was covered in a 13 μm PTFE film (American Durafilm, Inc.) and then was inserted into the electrolyte for collecting the Raman spectra. The cell was heated with a PID controller to 60 °C. Au wire (1 mm, Thermo Scientific) was used as the working electrode with Ni wire serving as the counter and Hg/HgO, calibrated in 30% w/w NaOH, as the reference electrode. A laser power of 5 mW cm^{-2} was used to excite the sample.

Author contributions:

Conceptualization: R.S., J.A.C., A.C.G., P.A.K.; Investigation: R.S., J.A.C., A.C.G., E.R., L.J.M., F.K., A.D.; Methodology: R.S., J.A.C., A.C.G., E.R., P.A.K.; Supervision: P.A.K., S.W.B.; Visualization: R.S., P.A.K.; Writing–original draft: R.S., P.A.K.; Writing–review & editing: R.S., P.A.K., S.W.B., A.D., F.K.

Conflicts of interest:

P.A.K. and S.W.B. have patented a process for producing iron metal and co-products from metal oxides (US18/329,849). P.A.K., R.S., J.A.C., and A.C.G. have filed a provisional patent on reprecipitation of iron ores.

Data availability:

Supplementary information is available with preparation of *pc*-Fe_2O_3, *an*-Fe_2O_3, *np*-Fe_3O_4, *np*-Fe_2O_3 and *prec*-Fe_3O_4 particles, composition of iron oxides and reduced iron films as characterized by EDX, additional SEM and TEM images, supporting discussion on impurities, and additional electrochemical characterization. The raw data used to prepare figures for the paper are available on GitHub (https://github.com/Kempler-Group/Magnetite2026). The model used for technoeconomic analysis and a list of assumptions with references has been provided in the Supplementary Information.

Acknowledgements:

This work was supported by the U.S. Department of Energy through the Office of Basic Energy Sciences under award DE-SC0023435. TEM results were partially supported by the National Science Foundation Division of Materials Research under Grant No. 2406393. We thank Joshua Razink and the Center for Advanced Materials Characterization in Oregon for assistance with preparing cross-sections for TEM, measurements, and analysis. E.R. conducted experiments on NaOH generation from chlor-iron cells and acknowledges support from Form Energy. We gratefully acknowledge Chemours for providing membranes for testing NaOH production in chlor-iron cells. We thank Janna Rathert, Joseph Manser, and James Smalley for helpful conversations on magnetite reactivity.

Notes and references:

(1) Liu, J.; Dong, D.; Caro, A. L.; Andreas, N. S.; Li, Z.; Qin, Y.; Bedrov, D.; Gao, T. Aqueous Electrolytes Reinforced by Mg and Ca Ions for Highly Reversible Fe Metal Batteries. *ACS Cent. Sci.* **2022**, *8* (6), 729–740. https://doi.org/10.1021/acscentsci.2c00293.

(2) Manohar, A. K.; Malkhandi, S.; Yang, B.; Yang, C.; Prakash, G. S.; Narayanan, S. R. A High-Performance Rechargeable Iron Electrode for Large-Scale Battery-Based Energy Storage. *J. Electrochem. Soc.* **2012**, *159* (8), A1209.

(3) Manohar, A. K.; Yang, C.; Malkhandi, S.; Prakash, G. S.; Narayanan, S. R. Enhancing the Performance of the Rechargeable Iron Electrode in Alkaline Batteries with Bismuth Oxide and Iron Sulfide Additives. *J. Electrochem. Soc.* **2013**, *160* (11), A2078.

(4) Fan, Z.; Friedmann, S. J. Low-Carbon Production of Iron and Steel: Technology Options, Economic Assessment, and Policy. *Joule* **2021**, *5* (4), 829–862.

(5) Gong, K.; Ma, X.; Conforti, K. M.; Kuttler, K. J.; Grunewald, J. B.; Yeager, K. L.; Bazant, M. Z.; Gu, S.; Yan, Y. A Zinc–Iron Redox-Flow Battery under $100 per kW h of System Capital Cost. *Energy Environ. Sci.* **2015**, *8* (10), 2941–2945.

(6) Dai, J.; Li, J.; Ling, F.; Yao, Y.; Wang, Y.; Ma, M.; Feng, J.; Xia, J.; Zhu, Y.; Yang, H. Unraveling the Degradation Mechanism of Sodium Iron Hexacyanoferrate Cathodes in Sodium Ion Batteries. *Energy Environ. Sci.* **2025**, *18* (19), 8791–8802.

(7) Raabe, D.; Tasan, C. C.; Olivetti, E. A. Strategies for Improving the Sustainability of Structural Metals. *Nature* **2019**, *575* (7781), 64–74.

(8) Zheng, X.; Paul, S.; Moghimi, L.; Wang, Y.; Vilá, R. A.; Zhang, F.; Gao, X.; Deng, J.; Jiang, Y.; Xiao, X.; Wu, C.; Greenburg, L. C.; Yang, Y.; Cui, Y.; Vailionis, A.; Kuzmenko, I.; Llavsky, J.; Yin, Y.; Cui, Y.; Dresselhaus-Marais, L. Correlating Chemistry and Mass Transport in Sustainable Iron Production. *Proc. Natl. Acad. Sci.* **2023**, *120* (43), e2305097120. https://doi.org/10.1073/pnas.2305097120.

(9) Geerdes, M.; Chaigneau, R.; Lingiardi, O. *Modern Blast Furnace Ironmaking: An Introduction (2020)*; Ios Press, 2020.

(10) Shen, L.; Qiao, Y.; Guo, Y.; Tan, J. Preparation and Formation Mechanism of Nano-Iron Oxide Black Pigment from Blast Furnace Flue Dust. *Ceram. Int.* **2013**, *39* (1), 737–744.

(11) Ma, Y.; Bae, J. W.; Kim, S.; Jovičević-Klug, M.; Li, K.; Vogel, D.; Ponge, D.; Rohwerder, M.; Gault, B.; Raabe, D. Reducing Iron Oxide with Ammonia: A Sustainable Path to Green Steel. *Adv. Sci.* **2023**, *10* (16), 2300111. https://doi.org/10.1002/advs.202300111.

(12) Ma, Y.; Souza Filho, I. R.; Zhang, X.; Nandy, S.; Barriobero-Vila, P.; Requena, G.; Vogel, D.; Rohwerder, M.; Ponge, D.; Springer, H.; Raabe, D. Hydrogen-Based Direct Reduction of Iron Oxide at 700°C: Heterogeneity at Pellet and Microstructure Scales. *Int. J. Miner. Metall. Mater.* **2022**, *29* (10), 1901–1907. https://doi.org/10.1007/s12613-022-2440-5.

(13) Mittal, S.; Davis, L. M. Rapid, Efficient Reduction of Iron Oxide with Ammonia. *Cell Rep. Phys. Sci.* **2025**, *6* (5).

(14) Kim, S.-H.; Zhang, X.; Ma, Y.; Souza Filho, I. R.; Schweinar, K.; Angenendt, K.; Vogel, D.; Stephenson, L. T.; El-Zoka, A. A.; Mianroodi, J. R. Influence of Microstructure and Atomic-Scale Chemistry on the Direct Reduction of Iron Ore with Hydrogen at 700 C. *Acta Mater.* **2021**, *212*, 116933.

(15) Choisez, L.; Hemke, K.; Özgün, Ö.; Pistidda, C.; Jeppesen, H.; Raabe, D.; Ma, Y. Hydrogen-Based Direct Reduction of Combusted Iron Powder: Deep Pre-Oxidation, Reduction Kinetics and Microstructural Analysis. *Acta Mater.* **2024**, *268*, 119752.
(16) Braun, T.; Wallace, C.; Pham, Q.; Nijhawan, S.; Alexander, C. L. Electrochemistry in Action: Iron and Steel Manufacturing. *Electrochem. Soc. Interface* **2024**, *33* (2), 38. https://doi.org/10.1149/2.F06242IF.
(17) Badalbayli, A.; Sinclair, N. S.; Kim, E.; Baker, A.; Akolkar, R. Electrochemical Recovery of Iron from Spent Pickle Liquor by Chloride-Based Molten Salt Electrolysis. *ECS Adv.* **2025**.
(18) Allanore, A.; Yin, L.; Sadoway, D. R. A New Anode Material for Oxygen Evolution in Molten Oxide Electrolysis. *Nature*, 2013, *497*, 353–356. https://doi.org/https://doi.org/10.1038/nature12134.
(19) Badalbayli, A.; Sinclair, N.; Kim, E.; Baker, A. A.; Akolkar, R. Editors' Choice—Molten Salt Electrolysis in Chloride Melts for Energy-Efficient Iron Metal Production. *J. Electrochem. Soc.* **2025**, *172* (3), 032508.
(20) Allanore, A.; Lavelaine, H.; Valentin, G.; Birat, J. P.; Lapicque, F. Iron Metal Production by Bulk Electrolysis of Iron Ore Particles in Aqueous Media. *J. Electrochem. Soc.* **2008**, *155* (9), E125.
(21) Allanore, A.; Lavelaine, H.; Valentin, G.; Birat, J. P.; Lapicque, F. Electrodeposition of Metal Iron from Dissolved Species in Alkaline Media. *J. Electrochem. Soc.* **2007**, *154* (12), E187.
(22) Fumo, A.; Lopes, D. V.; Starykevich, M.; Kovalevsky, A. V. Electroreduction of Magnetite for Steel Production from Ceramic Suspensions Containing Metallic Iron. *J. Electrochem. Soc.* **2025**, *172* (1), 012506.
(23) Noble, B. B.; Konovalova, A.; Moutarlier, L. J.; Brogden, V.; Kempler, P. A. Electrochemical Chlor-Iron Process for Iron Production from Iron Oxide and Salt Water. *Joule* **2024**, *8* (3), 714–727.
(24) Konovalova, A.; Goldman, A. C.; Shekhar, R.; Triplett, I.; Moutarlier, L. J.; Kwak, M.; Kempler, P. A. Pathways to Electrochemical Ironmaking at Scale Via the Direct Reduction of Fe_2O_3. *ACS Energy Lett.* **2025**, *10* (4), 1851–1857. https://doi.org/10.1021/acsenergylett.5c00166.
(25) LeDuc, J. A. M.; Loftfield, R. E.; Vaaler, L. E. Electrolytic Iron Powder from a Caustic Soda Solution. *J. Electrochem. Soc.* **1959**, *106* (8), 659.
(26) Nikolaeva, N. V.; Aleksandrova, T. N.; Chanturiya, E. L.; Afanasova, A. Mineral and Technological Features of Magnetite–Hematite Ores and Their Influence on the Choice of Processing Technology. *ACS Omega* **2021**, *6* (13), 9077–9085. https://doi.org/10.1021/acsomega.1c00129.
(27) He, Z.; Gudavarthy, R. V.; Koza, J. A.; Switzer, J. A. Room-Temperature Electrochemical Reduction of Epitaxial Magnetite Films to Epitaxial Iron Films. *J. Am. Chem. Soc.* **2011**, *133* (32), 12358–12361. https://doi.org/10.1021/ja203975z.
(28) Majid, A. I.; Finotello, G.; van der Schaaf, J.; Deen, N. G.; Tang, Y. On the Formation of Dendritic Iron from Alkaline Electrochemical Reduction of Iron Oxide Prepared for Metal Fuel Applications. *Chem. Eng. Sci.* **2024**, *291*, 119931.
(29) Shekhar, R.; Mukhopadhyay, S.; Sanchez, F.; Konovalova, A.; Boettcher, S. W.; Devaraj, A.; Kempler, P. A. Nanoporous Fe_2O_3 and Soluble Fe(II) Intermediates Accelerate the

Electrodeposition of Fe in NaOH(Aq). *ACS Nano* **2025**, *19* (37), 33449–33459. https://doi.org/10.1021/acsnano.5c10559.
(30) Allanore, A.; Lavelaine, H.; Valentin, G.; Birat, J. P.; Delcroix, P.; Lapicque, F. Observation and Modeling of the Reduction of Hematite Particles to Metal in Alkaline Solution by Electrolysis. *Electrochimica Acta* **2010**, *55* (12), 4007–4013.
(31) Spreitzer, D.; Schenk, J. Reduction of Iron Oxides with Hydrogen—A Review. *Steel Res. Int.* **2019**, *90* (10), 1900108. https://doi.org/10.1002/srin.201900108.
(32) Wang, C.; Baer, D. R.; Amonette, J. E.; Engelhard, M. H.; Antony, J.; Qiang, Y. Morphology and Electronic Structure of the Oxide Shell on the Surface of Iron Nanoparticles. *J. Am. Chem. Soc.* **2009**, *131* (25), 8824–8832. https://doi.org/10.1021/ja900353f.
(33) Cabot, A.; Puntes, V. F.; Shevchenko, E.; Yin, Y.; Balcells, L.; Marcus, M. A.; Hughes, S. M.; Alivisatos, A. P. Vacancy Coalescence during Oxidation of Iron Nanoparticles. *J. Am. Chem. Soc.* **2007**, *129* (34), 10358–10360. https://doi.org/10.1021/ja072574a.
(34) Sugimoto, T.; Wang, Y.; Itoh, H.; Muramatsu, A. Systematic Control of Size, Shape and Internal Structure of Monodisperse α-Fe2O3 Particles. *Colloids Surf. Physicochem. Eng. Asp.* **1998**, *134* (3), 265–279.
(35) Sugimoto, T.; Matijević, E. Formation of Uniform Spherical Magnetite Particles by Crystallization from Ferrous Hydroxide Gels. *J. Colloid Interface Sci.* **1980**, *74* (1), 227–243.
(36) Hofmann, M.; Müller, R.; Christidis, A.; Fischer, P.; Klaucke, F.; Vomberg, S.; Tsatsaronis, G. Flexible and Economical Operation of Chlor-alkali Process with Subsequent Polyvinyl Chloride Production. *AIChE J.* **2022**, *68* (1), e17480. https://doi.org/10.1002/aic.17480.
(37) Klaucke, F.; Müller, R.; Hofmann, M.; Weigert, J.; Fischer, P.; Vomberg, S.; Tsatsaronis, G.; Repke, J.-U. Chlor-Alkali Process with Subsequent Polyvinyl Chloride Production─Cost Analysis and Economic Evaluation of Demand Response. *Ind. Eng. Chem. Res.* **2023**, *62* (19), 7336–7351. https://doi.org/10.1021/acs.iecr.2c04188.
(38) Editor, S. I. N. *World Steel Pricing vs. U.S. Domestic Steel Pricing: Market Dynamics in the Era of 50% Tariffs*. Steel Industry News. https://steelindustry.news/world-steel-pricing-vs-u-s-domestic-steel-pricing-market-dynamics-in-the-era-of-50-tariffs/ (accessed 2025-12-08).
(39) Mike. *Hydrochloric Acid price index*. businessanalytiq. https://businessanalytiq.com/procurementanalytics/index/hydrochloric-acid-price-index/ (accessed 2025-12-08).
(40) *Electric Power Monthly - U.S. Energy Information Administration (EIA)*. https://www.eia.gov/electricity/monthly/epm_table_grapher.php?t=epmt_5_03 (accessed 2025-12-08).
(41) *European Wholesale Electricity Price Data*. Ember. https://ember-energy.org/data/european-wholesale-electricity-price-data (accessed 2025-12-08).
(42) *Power costs drop in China, helping tariff-hit industry*. Tech in Asia. https://www.techinasia.com/news/power-costs-drop-china-helping-tariffhit-industry (accessed 2025-12-08).
(43) Choisez, L.; Hemke, K.; Özgün, Ö.; Pistidda, C.; Jeppesen, H.; Raabe, D.; Ma, Y. Hydrogen-Based Direct Reduction of Combusted Iron Powder: Deep Pre-Oxidation, Reduction Kinetics and Microstructural Analysis. *Acta Mater.* **2024**, *268*, 119752.
(44) Arumugam, D.; Zhou, T.; Jagadeesan, S. N.; Pidathala, R. T.; Zhang, L.; Abeykoon, A. M.; Kwon, G.; Olds, D.; Narayanan, B.; Teng, X. Electrochemical Reduction Pathways from Goethite to Green Iron in Alkaline Solution with Silicate Additive. *ACS Sustain. Chem. Eng.* **2025**, *13* (7), 2633–2640. https://doi.org/10.1021/acssuschemeng.4c08451.

(45) Feynerol, V.; Lavelaine, H.; Marlier, P.; Pons, M.-N.; Lapicque, F. Reactivity of Suspended Iron Oxide Particles in Low Temperature Alkaline Electrolysis. *J. Appl. Electrochem.* **2017**, *47* (12), 1339–1350. https://doi.org/10.1007/s10800-017-1127-5.
(46) Boehme, C.; Starykevich, M.; Constantinescu, G.; Kovalevsky, A. V.; Lopes, D. V. Low-Temperature Electrowinning of Iron from Mixed Hematite-Magnetite Alkaline Suspensions. *J. Electrochem. Soc.* **2023**, *170* (5), 052502.
(47) Fumo, A.; Lopes, D. V.; Starykevich, M.; Kovalevsky, A. V. Electroreduction of Magnetite for Steel Production from Ceramic Suspensions Containing Metallic Iron. *J. Electrochem. Soc.* **2025**, *172* (1), 012506.
(48) Monteiro, J. F.; Ivanova, Y. A.; Kovalevsky, A. V.; Ivanou, D. K.; Frade, J. R. Reduction of Magnetite to Metallic Iron in Strong Alkaline Medium. *Electrochimica Acta* **2016**, *193*, 284–292.
(49) De Faria, D. L. A.; Venâncio Silva, S.; De Oliveira, M. T. Raman Microspectroscopy of Some Iron Oxides and Oxyhydroxides. *J. Raman Spectrosc.* **1997**, *28* (11), 873–878. https://doi.org/10.1002/(SICI)1097-4555(199711)28:11%3C873::AID-JRS177%3E3.0.CO;2-B.
(50) Chamritski, I.; Burns, G. Infrared- and Raman-Active Phonons of Magnetite, Maghemite, and Hematite: A Computer Simulation and Spectroscopic Study. *J. Phys. Chem. B* **2005**, *109* (11), 4965–4968. https://doi.org/10.1021/jp048748h.
(51) Frierdich, A. J.; Helgeson, M.; Liu, C.; Wang, C.; Rosso, K. M.; Scherer, M. M. Iron Atom Exchange between Hematite and Aqueous Fe(II). *Environ. Sci. Technol.* **2015**, *49* (14), 8479–8486. https://doi.org/10.1021/acs.est.5b01276.
(52) Gorski, C. A.; Handler, R. M.; Beard, B. L.; Pasakarnis, T.; Johnson, C. M.; Scherer, M. M. Fe Atom Exchange between Aqueous Fe^{2+} and Magnetite. *Environ. Sci. Technol.* **2012**, *46* (22), 12399–12407. https://doi.org/10.1021/es204649a.
(53) Lee, D.-C.; Lei, D.; Yushin, G. Morphology and Phase Changes in Iron Anodes Affecting Their Capacity and Stability in Rechargeable Alkaline Batteries. *ACS Energy Lett.* **2018**, *3* (4), 794–801. https://doi.org/10.1021/acsenergylett.8b00063.
(54) Amaral, S. T.; Muller, I. L. Effect of Silicate on Passive Films Anodically Formed on Iron in Alkaline Solution as Studied by Electrochemical Impedance Spectroscopy. *Corrosion* **1999**, *55* (1), 17–23.
(55) Hasson, D.; Shemer, H.; Semiat, R. Removal of Scale-Forming Ions by a Novel Cation-Exchange Electrochemical System—A Review. *Desalination Water Treat.* **2016**, *57* (48–49), 23147–23161.
(56) Kirschen, M.; Hay, T.; Echterhof, T. Process Improvements for Direct Reduced Iron Melting in the Electric Arc Furnace with Emphasis on Slag Operation. *Processes* **2021**, *9* (2), 402.
(57) Rosner, F.; Papadias, D.; Brooks, K.; Yoro, K.; Ahluwalia, R.; Autrey, T.; Breunig, H. Green Steel: Design and Cost Analysis of Hydrogen-Based Direct Iron Reduction. *Energy Environ. Sci.* **2023**, *16* (10), 4121–4134. https://doi.org/10.1039/D3EE01077E.
(58) IRENA. *Green Hydrogen Cost Reduction*; IRENA, 2020. https://www.irena.org/Publications/2020/Dec/Green-hydrogen-cost-reduction (accessed 2023-05-24).
(59) Papadias, D. D.; Ahluwalia, R. K. Bulk Storage of Hydrogen. *Int. J. Hydrog. Energy* **2021**, *46* (70), 34527–34541. https://doi.org/10.1016/j.ijhydene.2021.08.028.

(60) Tan, Y.; Yang, H.; Tian, G.; Yu, X.; Hu, J.; Wang, X.; Cheng, J.; Song, H. Research Progress and Trends in Iron Metal Purification Processes. *Ind. Eng. Chem. Res.* **2023**, *62* (12), 4817–4830. https://doi.org/10.1021/acs.iecr.3c00132.